Cell Reports
Methods

Report

Single-cell sequencing of individual retinal organoids reveals determinants of cell-fate heterogeneity

Graphical abstract

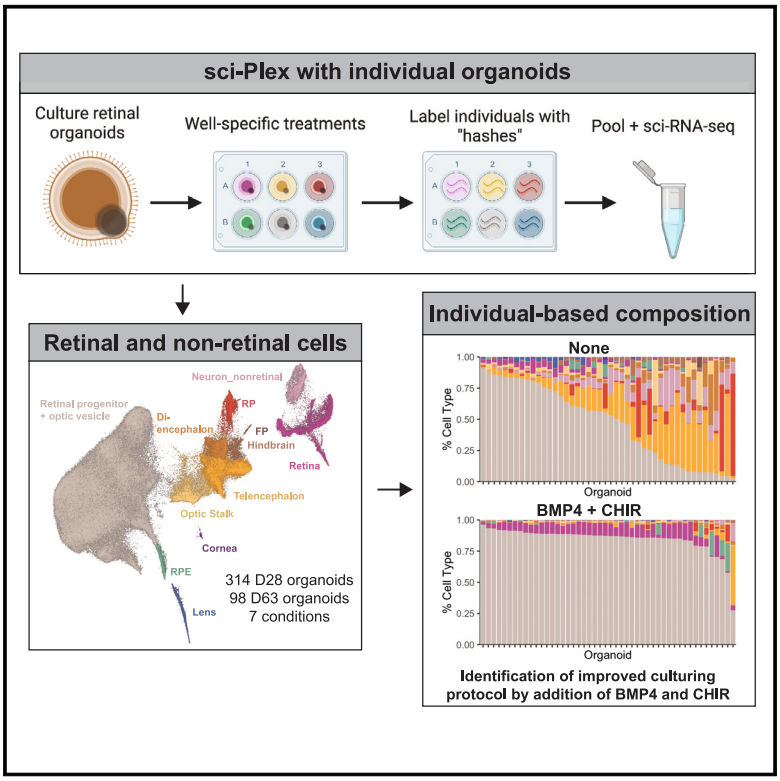

Highlights

- Hundreds of individual retinal organoids sequenced at single-cell resolution
- Detection of significant changes in cell-type abundance and heterogeneity
- Wnt and BMP signaling activation increases retinal cell abundance

Authors

Amy Tresenrider, Akshayalakshmi Sridhar, Kiara C. Eldred, Sophia Cuschieri, Dawn Hoffer, Cole Trapnell, Thomas A. Reh

Correspondence

coletrap@uw.edu (C.T.), tomreh@uw.edu (T.A.R.)

In brief

Tresenrider et al. adapt the single-cell sequencing-based multiplexing strategy sci-Plex to assay the composition and heterogeneity of 410 individual retinal organoids after the perturbation of developmental signaling pathways. They find that the activation of BMP and Wnt signaling improves retinal organoid composition.

Tresenrider et al., 2023, Cell Reports Methods 3, 100548
August 28, 2023
https://doi.org/10.1016/j.crmeth.2023.100548

CellPress

Cell Reports Methods

CellPress
OPEN ACCESS

Report

Single-cell sequencing of individual retinal organoids reveals determinants of cell-fate heterogeneity

Amy Tresenrider,[1] Akshayalakshmi Sridhar,[2,5] Kiara C. Eldred,[2,5] Sophia Cuschieri,[2] Dawn Hoffer,[2] Cole Trapnell,[1,3,4,*] and Thomas A. Reh[2,6,*]

[1]Department of Genome Sciences, University of Washington, Seattle, WA 98195, USA
[2]Department of Biological Structure, University of Washington, Seattle, WA 98195, USA
[3]Brotman Baty Institute for Precision Medicine, University of Washington, Seattle, WA 98195, USA
[4]Allen Discovery Center for Cell Lineage Tracing, Seattle, WA 98195, USA
[5]These authors contributed equally
[6]Lead contact
*Correspondence: coletrap@uw.edu (C.T.), tomreh@uw.edu (T.A.R.)
https://doi.org/10.1016/j.crmeth.2023.100548

MOTIVATION The gaining popularity of organoids for the study of human development and disease will require technologies that advance the scale and depth by which they can be analyzed. In current retinal organoid protocols, high organoid heterogeneity is a critical but poorly understood reality. By adapting the single-nucleus RNA-seq multiplexing technique sci-Plex to assay the cell-type composition and heterogeneity of hundreds of individual retinal organoids, our method provides an unparalleled look at the factors driving heterogeneity and serves as a tool to screen for better culturing protocols.

SUMMARY

With a critical need for more complete *in vitro* models of human development and disease, organoids hold immense potential. Their complex cellular composition makes single-cell sequencing of great utility; however, the limitation of current technologies to a handful of treatment conditions restricts their use in screens or studies of organoid heterogeneity. Here, we apply sci-Plex, a single-cell combinatorial indexing (sci)-based RNA sequencing (RNA-seq) multiplexing method to retinal organoids. We demonstrate that sci-Plex and 10× methods produce highly concordant cell-class compositions and then expand sci-Plex to analyze the cell-class composition of 410 organoids upon modulation of critical developmental pathways. Leveraging individual organoid data, we develop a method to measure organoid heterogeneity, and we identify that activation of Wnt signaling early in retinal organoid cultures increases retinal cell classes up to 6 weeks later. Our data show sci-Plex's potential to dramatically scale up the analysis of treatment conditions on relevant human models.

INTRODUCTION

There has been good progress developing *in vitro* systems that recapitulate the structure and function of a variety of organs.[1–9] Retinal organoids, for example, contain all the major retinal neuronal and glial (Müller glia) cell classes and follow the developmental timing and laminar organization of the retina.[10] Importantly, retinal organoids represent an accessible and renewable *in vitro* system for studies of development[11] and disease progression. When generated from patient induced pluripotent stem cells (iPSCs), retinal organoids model patient-specific disease phenotypes,[12,13] with applications in personalized medicine or for cell replacement in degenerative diseases.[14–16]

However, several roadblocks limit the full potential of organoids, including organoid-to-organoid heterogeneity, batch effects, and high costs.[17] While several well-established protocols exist for retinal organoid generation, most protocols require manual selection or dissection of organoids.[18,19] A protocol has been developed that eliminates the need for dissection, but it relies on specialized micro-well plates that have not been widely adopted, and it still only produces ~80% retinal organoids.[20] For this reason, the presence of non-retinal cells in retinal organoid cultures, in an unpredictable and heterogeneous manner, limits their reproducibility, especially for large-scale experiments.[18,19,21]

To advance the standardization of retinal organoids, we developed a high-throughput single-cell sequencing-based screening

pipeline. Current techniques for screening in organoids rely on microscopy-based approaches that implement measurements of size and morphology, use viability stains, and/or perform immunostaining/fluorescence for a small number of marker genes.[22–25] Single-cell sequencing reveals the full array of cell classes, permits the discovery of unpredictable cellular states, and allows for a treatment's effect to be measured across all cell types. However, the high per-sample cost cannot practically scale past a handful of conditions (Table S1). sci-Plex, which builds upon single-cell combinatorial indexing-based RNA sequencing (sci-RNA-seq), facilitates the labeling and simultaneous processing of thousands of conditions with a single-cell output.[26] Originally performed in culture, sci-Plex was recently applied to thousands of individual zebrafish embryos exposed to genetic or temperature-based perturbations.[27,28] A handful of studies have sequenced individual organoids, but their experimental designs and level of replication are sharply constrained by the cost and throughput of droplet-based single-cell sequencing technologies.[29,30] By contrast, sci-Plex increases the capacity to process individual organoids at single-cell resolution and enables the development of protocols that better recapitulate *in vivo* development.

Here, we demonstrate the first application of sci-Plex in organoids. To confirm the validity of the method, we show strikingly similar cell-class compositions of matched bulk retinal organoids prepared by sci-Plex compared with commercially available droplet-based single-cell sequencing methods. We then perform sci-Plex on 410 individual organoids while modulating key developmental signaling pathways. We find that activation of BMP followed by Wnt signaling produces organoids with a greater proportion of retinal cells compared with BMP activation alone without increasing organoid-to-organoid heterogeneity. With the depth of information obtained across hundreds of individuals, we vastly expand the types of analyses possible in single-cell sequencing-based methods in organoids, and we identify a culturing protocol that improves the composition of retinal organoids.

RESULTS

Successful multiplexing of retinal organoids using sci-Plex

To demonstrate that multiplexed samples from sci-Plex have cell-class compositions (1) comparable to those recovered using commercial droplet-based techniques and (2) that would be expected developmentally, retinal organoids cultured for 29, 78, or 185 days were dissociated into single-cell suspensions and split for processing by either the 10× Chromium platform or sci-Plex (Figures 1A and S1A). sci-Plex recovered 12,867 cells (median unique molecular identifiers [UMIs] for day 29: 5,512, day 78: 5,797, day 185: 5,695.5), and 10× recovered 16,914 (median UMI for day 29: 6,335, day 78: 4,118, day 185: 3,950) (Figures S1B–S1H). Using the hash barcodes, the sample from which a cell originated was determined for 95% of the cells (Figures S1D and S1E).

The retina develops in a highly coordinated way with all retinal neurons and the Müller glia (MG) arising from a shared retinal progenitor cell (RPC) population[31](Figure 1D) with conserved developmental timing between human retinal organoids and the fetal retina[10] (Figure 1E). Staining of retinal organoids supported previous observations indicating that the layered organization of the retina is maintained[10] (Figure 1F). We used the knowledge of developmental timing to determine how well sci-Plex segregated samples of differing ages (Figures 1B, 1G, and S1K). As expected, day 29 organoids included mainly RPCs, differentiating retinal ganglion cells (RGCs), other retinal neuron precursors, and brain progenitor cells (Figures 1C, 1G, S1J, and S1K; see Table S2 for marker genes). Day 78 organoids had far more RGCs and horizontal, amacrine, and photoreceptor precursor cells (Figures 1C, 1G, and S1K). By day 185, rods, cones, and bipolar cells were dominant (Figures 1C, 1G, S1J, and S1K). MG and astrocyte clusters were also defined (Figures 1B, 1C, 1G, S1J, and S1K). Comparing directly between 10× and sci-Plex, the cell-class distribution was highly concordant, although some low-abundance cell classes were detected more frequently in sci-Plex, possibly due to differences between nuclear and whole-cell transcript recovery (Figure 1G). We also found that processing just the sci-Plex data using Monocle3 resulted in a comparable cell-class classification (Figures S1L–S1N). These analyses demonstrated that sci-Plex can both identify a cell's well of origin and correctly assign its cell type.

Detection of cell-class abundance changes across treatments through multiplexing of individual organoids

We next aimed to use the multiplexing ability of sci-Plex to screen conditions that modulate signaling pathways to (1) better understand the effect signaling pathways have on cell-fate decisions in young retinal organoids and (2) use this information to design better organoid differentiation protocols. The BMP, Sonic hedgehog, Wnt, and fibroblast growth factor (FGF) signaling pathways are all key regulators of eye and brain development.[32,33] Modulators of these pathways, BMP4 (BMP protein), SAG (Sonic hedgehog agonist), CHIR99021 (Wnt agonist), and SU5402 (FGF inhibitor), have all been used in published retinal organoid protocols.[19] However, there is no agreed upon "best" combination of these factors.

To perform a systematic and quantitative analysis, sci-Plex was used to label 314 individual organoids from seven different treatment conditions. Organoids were prepared for sci-Plex 28 days after initiation of differentiation (Figures 2A and 2B). No selection of organoids that morphologically appeared retinal was applied, as we aimed to understand the factors driving the heterogeneity that obligates such selection steps. An early time point was chosen to better understand the effects of signaling modulation on the choice between retinal and non-retinal fates. We distributed the organoids into 96-well plates with each well harboring a single organoid, permitting the hash-based barcoding to be performed on individuals. After hashing, cells were subjected to sci-RNA-seq3, a version of combinatorial indexing that greatly increases the throughput of the method.[34] After filtering, 203,511 cells (median UMI: 350) were recovered (Figures S2A–S2F) with a median of 505 cells per individual (Figure 2C). Our successful recovery of cells from hundreds of individual organoids set us up to perform statistical analyses relating to cell-class abundance and organoid-to-organoid heterogeneity in an unprecedented manner.

CellPress
OPEN ACCESS

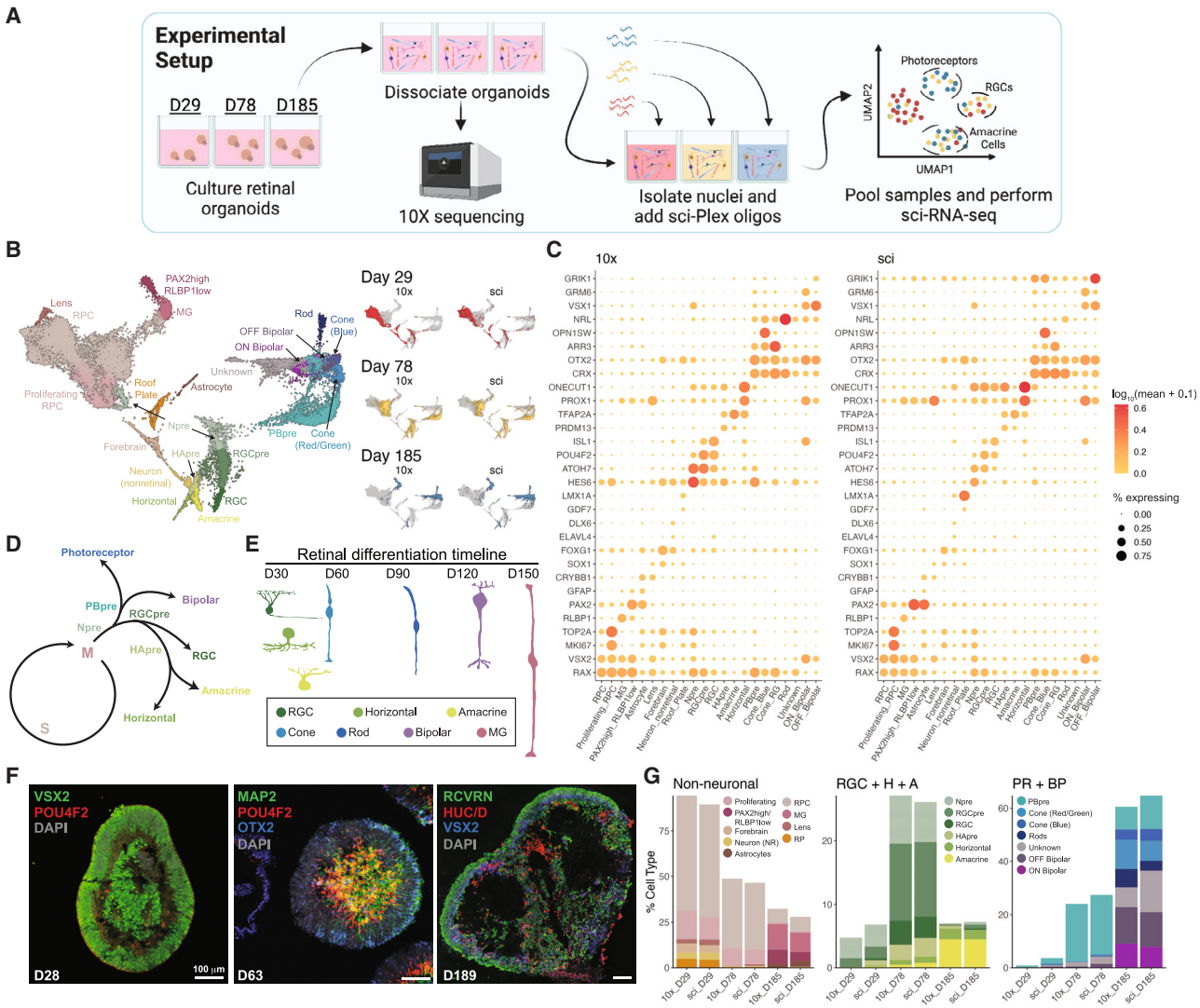

Figure 1. Comparison between sci-Plex and 10×

(A) Retinal organoids were cultured for 29, 78, or 185 days. The cells were split and either processed by a 10× RNA-seq pipeline or prepared by sci-Plex.

(B) Integrated UMAP of sci-Plex and 10× datasets. Left: cells colored by cell type. RPC, retinal progenitor cell; MG, Müller glia; Npre, retinal neuronal precursor; RGC, retinal ganglion cell; RGCpre, RGC precursor; HApre, horizontal/amacrine precursor; PBpre, photoreceptor/bipolar precursor. Right: cells are faceted by organoid age and technology. Cells are colored by age.

(C) Dot plot of genes used to define cell types in (B). Dot size indicates the percentage of cells that express the gene of interest. Color indicates the log10 mean UMIs per cell.

(D) Representation of retinal neuron developmental trajectories.

(E) Timeline of retinal cell differentiation in human organoids.

(F) Immunostaining of day 28, 63, and 189 organoids for progenitor (VSX2-day 28), RGC (POU4F2), photoreceptor/bipolar (OTX2), neuronal (MAP2), amacrine/horizontal/RGC (HuC/D), bipolar cell (VSX2-day 189), and photoreceptor (RCVRN) markers. Scale bar represents 100 μm.

(G) Using the cell-type assignments from (B), cells were counted, and the percentage of cell type was determined for each technology and organoid age.

Despite the lower UMI counts with sci-RNA-seq3, cell classes were readily defined with clustering followed by the analysis of marker gene expression (Figures 2D, 2E, and S2H; Table S2). The largest population of cells was the RPC/optic vesicle (RPC_OV), but we also recovered retinal neuron precursors and non-retinal cells (Figures 2D, 2E, and S2G). RPC_OV cells dramatically decreased in the sonic hedgehog (SHH) activation (SAG) treatment when compared with the "None" treatment (no exposure to any of the signaling modulators), yet they increased in the BMP, SU5402, CHIR, and SU5402:CHIR treatments (Figures 2E–2G). At this time point, large changes in cell composition were apparent, but smaller changes in cell-class abundance were not.

We next aimed to use statistical methods to assess treatment-dependent changes across all cell classes. We harnessed the

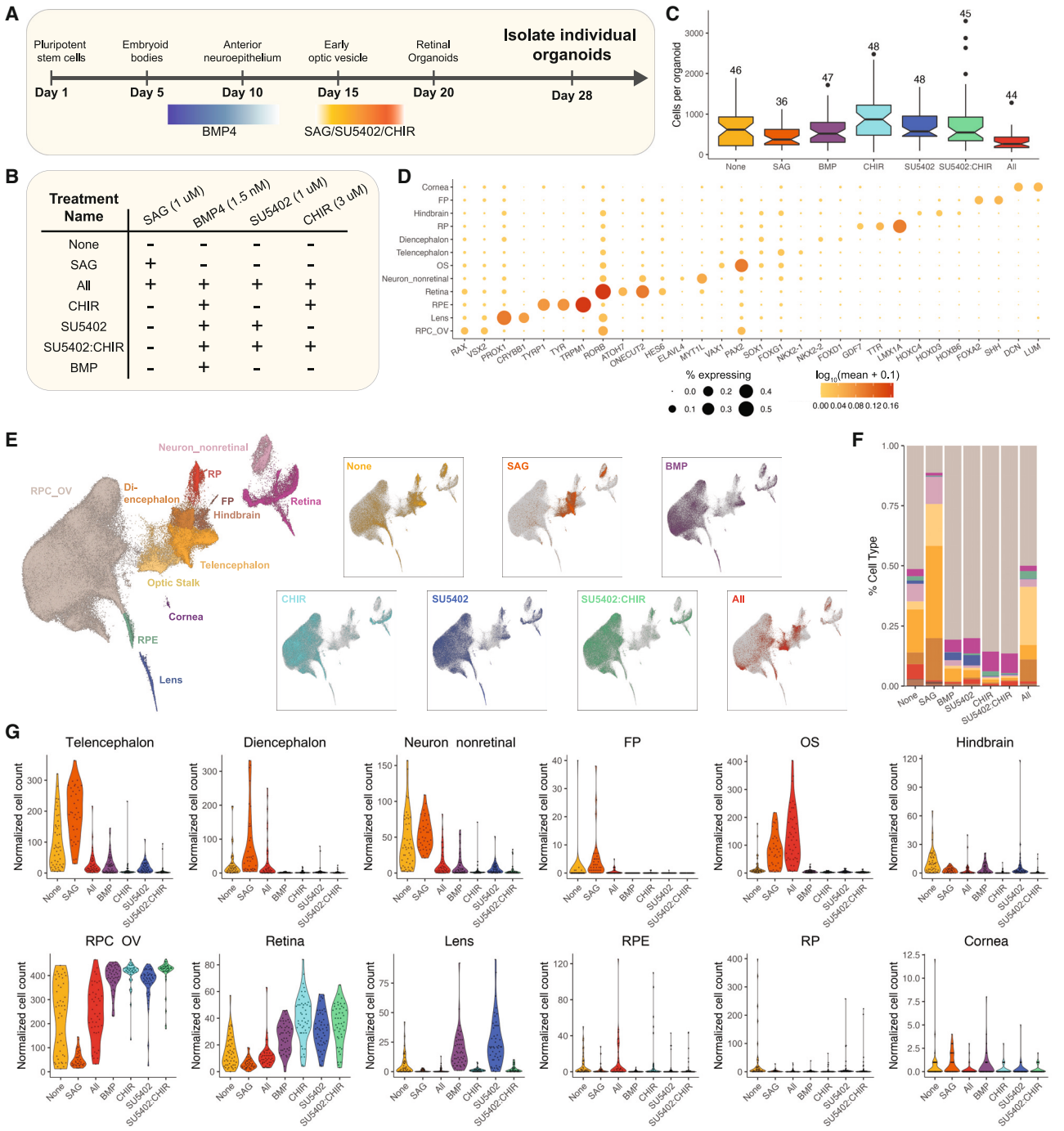

Figure 2. sci-Plex applied to individual organoids after signaling pathway modulation

(A) Overview of the retinal organoid differentiation protocol.

(B) A summary of the seven treatments performed.

(C) Boxplot of the number of cells recovered per organoid for each treatment. Number above the boxplot indicates the number of individual organoids in which >50 cells were recovered for that treatment. The notch of the boxplots represents the median cells per organoid. The colored region indicates the values from the lower 25th to the upper 75th quartile of cell counts. The whiskers span the range of the cell counts within 1.5× the distance between the 25th–75th percentiles. Points outside of that range are displayed as outliers.

(D) Dot plot of the genes used to define cell types for day 28 organoids. Dot size indicates the percentage of cells expressing the gene of interest. Color indicates the log10 mean UMIs per cell.

(legend continued on next page)

power of our individual organoid data to fit a statistical model using the beta-binomial distribution (STAR Methods).[27,28] Our model found that the organoids from treatments that include addition of BMP4, with the exception of "All" (exposure to all of the signaling modulators), produced significantly more RPC_OV and retinal cells compared with None (Figures 2G and 3A). This supports previous reports indicating that the addition of BMP4 improves the efficiency of retinal differentiation from stem cells.[18] We also saw that SHH activation decreased RPC_OV cell counts and significantly increased diencephalon, telencephalon, optic stalk, and non-retinal neurons (Figure 3A). Interestingly, the optic stalk was significantly increased in the All treatment (Figure 3A). Thus, with our well-powered experiment and statistical approach, we were able to interpret cell-class-level effects from each treatment.

To better investigate whether SU5402, CHIR, or SU5402:CHIR led to improvements over BMP4 alone, we trained a new model comparing these groups. In contrast to the addition of BMP4 alone, the addition of BMP4 combined with Wnt activation (CHIR, SU5402:CHIR) caused a striking loss of lens cells (Figure 3B). Both treatments with Wnt activation also robustly decreased most other non-retinal cell classes (Figure 3B). Of the conditions with high RPC_OV cell counts, CHIR treatment led to the highest relative numbers of retinal pigmented epithelium (RPE) cells in the organoids, consistent with prior evidence that Wnt activation steers cells toward the RPE fate both *in vivo* and *in vitro*.[35,36] Unexpectedly, both the CHIR and SU5402:CHIR treatments increased neural retinal cell counts (Figure 3B). Overall, our results indicated that the addition of CHIR99021 to the culturing protocol increased the retinal content of organoids compared with the addition of BMP4 only.

To determine whether any of the treatments affected the production of specific retinal cell classes, we selected only the RPC_OV and retinal cells and carried out dimensionality reduction, clustering, and cell-type annotation using marker genes (Figures S3A–S3C; Table S2). We found that CHIR, SU5402, and SU5402:CHIR treatments increased photoreceptor/bipolar cell precursors (PBpres) (Figures S3D and S3E). CHIR and SU5402:CHIR treatments also significantly increased neurogenic precursor (Npre) cells (Figures S3D and S3E). Overall, the results of this experiment showed that exposure to CHIR99021 reduced non-retinal cell classes, increased retinal cells, and may have specifically enhanced photoreceptor/bipolar cell production.

Cell abundance changes detected by sci-Plex are concordant with immunostaining

To further investigate our observations from sci-Plex, we performed immunostaining on cryosections from matched day 27 organoids (Figure S3F). Consistent with the sci-Plex results, we observed a significant increase in PAX2+ optic stalk-like regions in the All treatment (Figure 3C). Also consistent with sci-Plex, we found significant increases in VSX2+ regions (RPCs and retinal neuron precursors) in CHIR- and SU5402:CHIR-treated organoids (Figure 3C). However, the immunolabeling results and sci-Plex did not agree when comparing the BMP and None treatments: sci-Plex showed an increase in VSX2+ regions, yet this was not apparent in the cryosectioned organoids. This suggests that the reduced number of organoids used for immunostaining hindered our ability to find some of the significant changes in cell composition that sci-Plex identified. Overall, we did not detect the same breadth of cell-class abundance changes by immunostaining; however, all significant changes detected with immunostaining were also observed by sci-Plex.

Organoid subtypes are identified within treatment groups

In order to quantify heterogeneity across organoids, we looked at the cell-class compositions of each individual. Recent innovations have increased the percentage of organoids in a given culture that are retinal, but the definition of retinal is based on qualitative bright-field images where variation is observable, and the molecular source of variation is not defined[18,19] (Figure 3D). Our individual organoid sci-Plex dataset provided a more quantitative picture of the variation that exists within and across treatments (Figures 3E–3L). Without exposure to any of the signaling modulators (None), organoids ranged from being primarily RPCs to almost completely non-retinal (Figure 3F). While BMP4 treatment markedly reduced the heterogeneity of the organoids (BMP, CHIR, SU5402, SU5402:CHIR) (Figures 3H–3K), a subset of the organoids demonstrated atypical cell-class distributions.

To define organoids within a culture that are divergent in their cell-class compositions, we developed a method to categorize organoids into "archetypes." We counted the number of cells of each type in each organoid and used the resulting normalized cell class × organoid matrix (see STAR Methods) to create a uniform manifold approximation and projection (UMAP) in which each of the points represented an individual organoid. We performed clustering and found that organoids of a given treatment fell predominantly into a single archetype (cluster) (Figures 3M, 3N, and S3G). We also became interested in why a specific secondary archetype may appear for one treatment and not another. For example, archetype 2, defined by high counts of hindbrain cells and non-retinal neurons, was higher for BMP than it was for the other high-retinal-cell-content treatments that had more organoids from archetype 5 (high RPE, high roof plate) (Figures 3M, 3N, and S3H). These cell classes (i.e., hindbrain, non-retinal neurons, RPE, and roof plate) were not seen as significantly increased compared to the BMP treatment (except for RPE in CHIR), yet they were compellingly present in high numbers for a small set of individuals (Figures 3B and 3H–3K). Together, these results show that sci-Plex can define the typical cellular composition of organoids and detect the way by which a minority of organoids within a given treatment deviate from the established typical cell-class composition.

(E) Left: UMAP of the recovered cells with cell-type annotations. Right: for each UMAP, cells from the specified treatment are colored. RPC_OV, retinal progenitor cell/optic vesicle; RPE, retinal pigmented epithelium; OS, optic stalk; RP, roof plate; FP, floor plate.
(F) Stacked bar plot with mean cell-type composition of day 28 organoids displayed for each treatment.
(G) Violin plots of size-factor-normalized cell counts for each cell type from day 28 organoids. Colored by treatment.

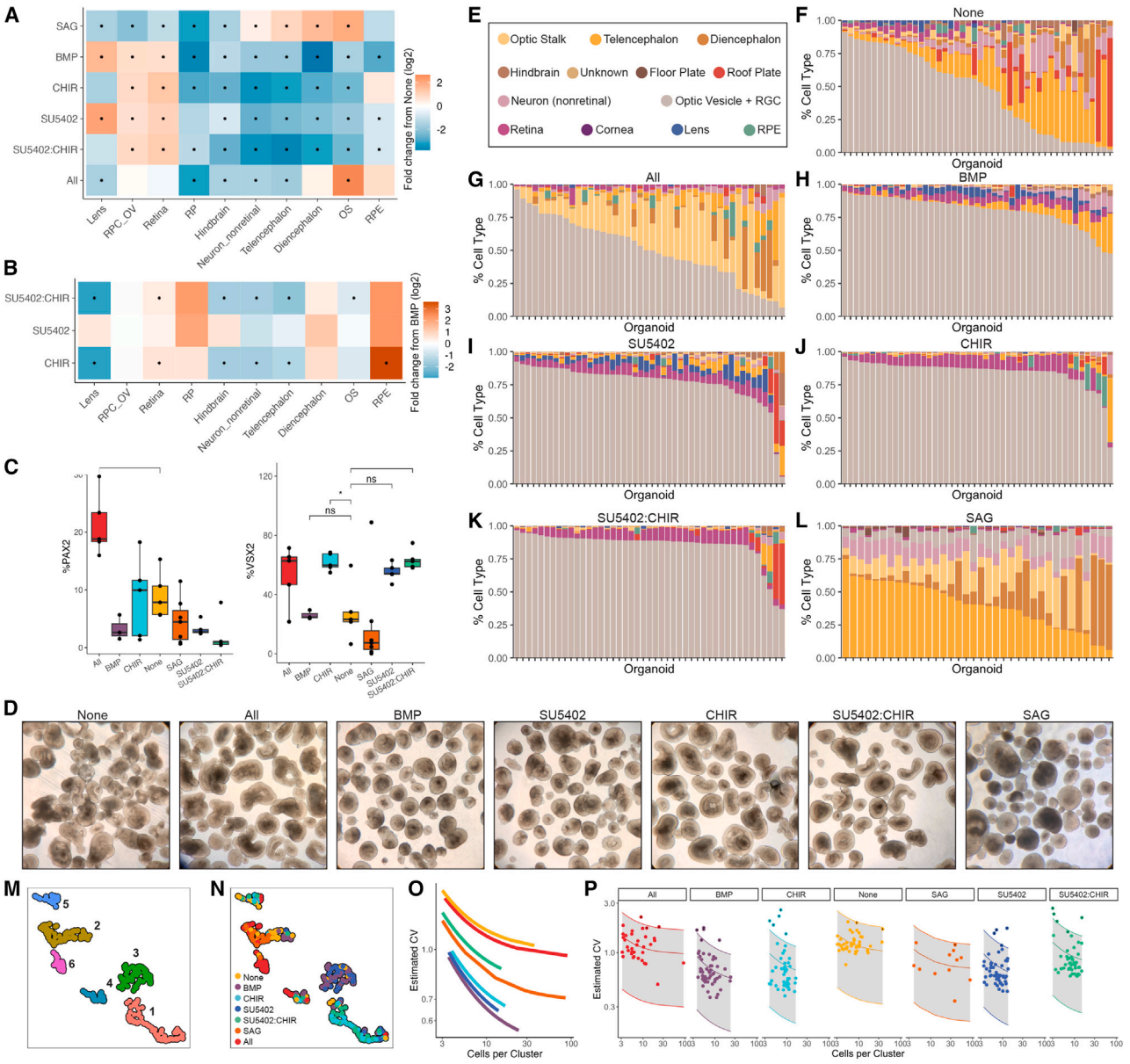

Figure 3. sci-Plex allows the detection of significant changes in cell-type abundance and heterogeneity

(A) Heatmap of fold change in cell-type abundance compared to "None" for day 28 organoids. The data was modeled using a beta-binomial distribution and significance was determined by a Wald test. An asterisk (*) in the center of the box indicates a q value of less than 0.05 after Benjamini-Hochberg correction.

(B) Heatmap of fold change in cell-type abundance compared with BMP for day 28 organoids. Statistical analysis was performed as in (A).

(C) Quantification of day 27 immunostained organoids. Significance was determined by performing t tests between the treatment of interest and None. Benjamini-Hochberg correction was performed to adjust the p value. *$p < 0.05$. The line of the boxplots represents the median cells per organoid. The colored region indicates the values from the lower 25th to the upper 75th quartile of cell counts. The whiskers span the range of the cell counts within 1.5× the distance between the 25th–75th percentiles.

(D) Bright-phase images of organoids the day before sci-Plex (day 27). Scale bars represent 200 μM.

(E) Cell-type legend for (F)–(L).

(F) Stacked bar plot, each bar represents an individual day 28 organoid exposed to the None treatment. Bars colored by cell-class composition.

(G–L) Same as (F) but for (G) All, (H) BMP, (I) SU5402, (J) CHIR, (K) SU5402:CHIR, and (L) SAG.

(M) UMAP generated using the size-factor-normalized cell type by organoid matrix generated from day 28 individual organoids. Colored by cluster.

(N) UMAP from (M) with the organoids colored by treatment.

(O) The mean and coefficient of variation (CV) were modeled for each cluster and each treatment. Displayed are the modeled relationships colored by treatment.

(P) Model from (O) faceted by treatment. The shaded area marks the range within 2 standard deviations from the mean. Points represent the individual cluster values.

CellPress
OPEN ACCESS

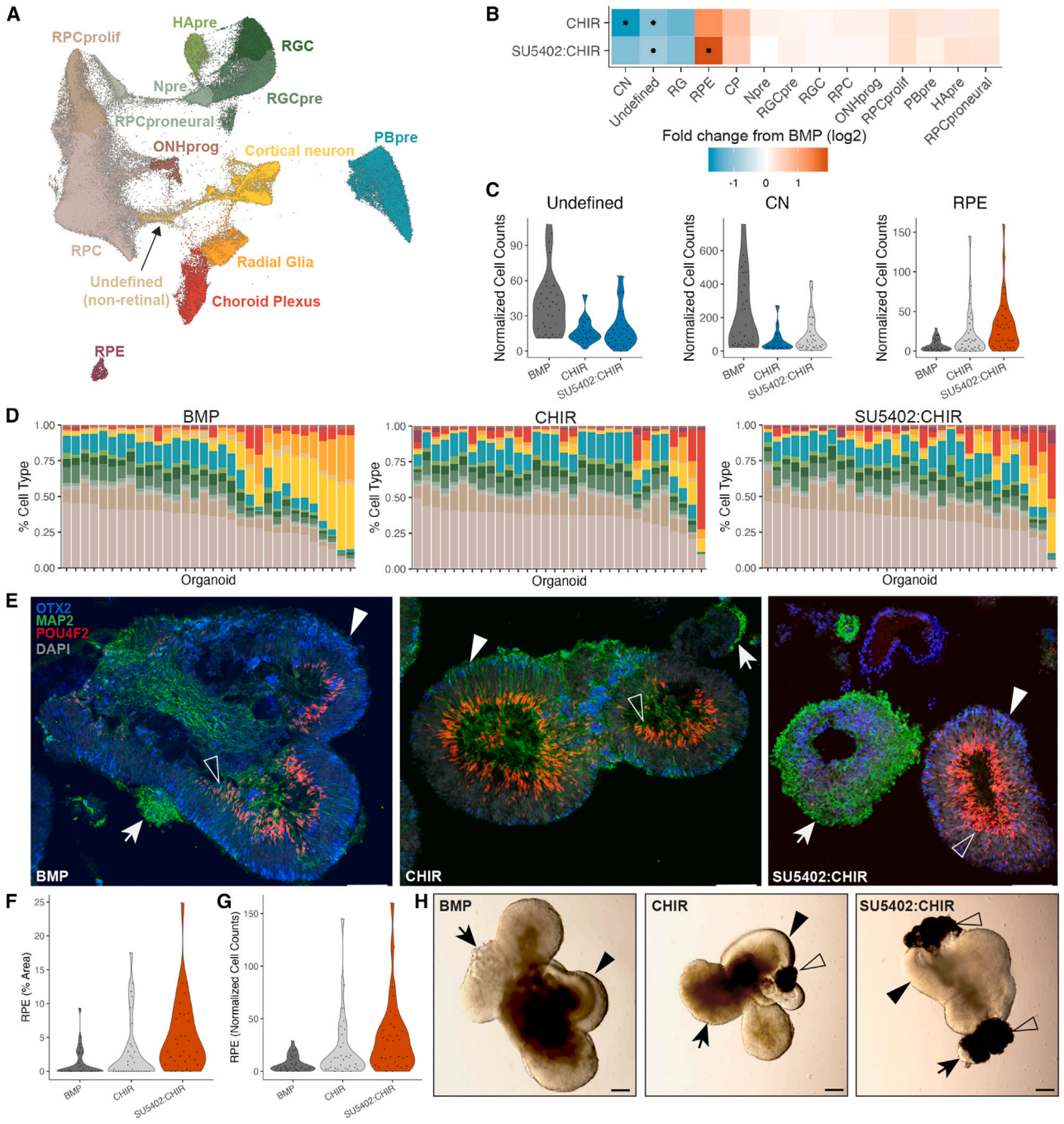

Figure 4. Day 63 organoids demonstrate continued perturbation by signaling modulation

(A) UMAP with cell-type annotations from individually hashed D63 organoids exposed to BMP, CHIR, and SU5402:CHIR treatments. RPCprolif, proliferating RPC; RPCproneural, proneural RPC; ONHprog, optic nerve head progenitor; CN, cortical neuron; RG, radial glia; CP, choroid plexus.

(B)Heatmap of fold change in cell-type abundance compared with BMP. The data was modeled using a beta-binomial distribution and significance was determined by a Wald test. An asterisk (*) in the center of the box indicates a q value of less than 0.05 after Benjamini-Hochberg correction.

(C) Violin plots of size-factor-normalized cell counts for day 63 organoids. Dark gray, control treatment in (B); light gray, no significant change; teal, significant decrease in abundance ($p < 0.05$); orange, significant increase in abundance ($p < 0.05$). Significance was determined as in (B).

(D) Stacked bar plots, each bar represents an individual organoid. Bars are colored by the cell-type composition. Right: cell-type color legend.

(legend continued on next page)

Statistical measurements of organoid heterogeneity identify treatments that decrease homogeneity

We next sought to quantify the variability in cell composition across treatments. We used a method that accounts for the mean-variance relationship in cell abundances across individuals as previously described.[27,28,37] Cells were divided into 67 clusters (as used to define cell classes) (Figure S3I). The variance and mean among individuals were calculated for each treatment within each cluster (see STAR Methods). After modeling, we plotted the relationship between the number of cells per cluster and the expected coefficient of variation (CV) (Figure 3O). Lines lower on the plot have a lower CV and thus less heterogeneity across clusters. Comparing BMP with each of the other treatments in a pairwise fashion, we used a likelihood ratio test on the models of variance with and without a treatment term in order to assess whether other treatments affected organoid heterogeneity. We found that CHIR and SU5402 treatments did not significantly increase heterogeneity compared with BMP (Table S3). Our modeling also enabled us to identify specific clusters of cells that have a higher CV than statistically expected (Figures 3P, S3J, and S3K). This most commonly included RPE and roof plate cells, followed by other non-retinal cell classes (Figures S3J and S3K). The analysis used a statistical method in a novel manner to find that the additional activation of Wnt or the inhibition of FGF signaling does not change a culture's homogeneity compared with treatment with BMP4 alone, but that all other treatments increase heterogeneity.

Early modulation of signaling pathways affects long-term cellular composition

To see whether the effects of signaling modulation carry forward as the cells differentiate into more mature fates, we performed sci-Plex on 96 individual organoids cultured for 63 days. After filtering, 194,335 hashed cells were recovered (median UMIs: 341, median features: 298) with a median of 1841.5 cells per organoid (Figures S4A–S4G). Cell classes were defined using marker genes (Figures 4A and S4H). Although RPCs and retinal neurons made up the majority of the cells, cells with brain characteristics persisted. Again, Wnt activation (CHIR, SU5402:CHIR) led to significant decreases in mean cell counts for non-retinal/cortical neurons and undefined cells (Figures 4B and 4C). In addition, there was a significant increase in RPE cells upon FGF inhibition and Wnt activation (SU5402:CHIR) (Figures 4B and 4C). At day 63, many retinal neuron cell classes, including PBpres, horizontal/amacrine precursors (HApres), proliferating RPCs (RPCprolifs), and proneural RPCs (RPCproneurals), were broadly increased in the CHIR and SU5402:CHIR treatments, when compared with BMP, but not to the level of significance (Figures 4B and S4I). Plotting the individual organoid cell composition (Figure 4D) also highlighted the fact that Wnt activation (CHIR) reduced the number of organoids containing high representation of cortical neurons when compared with BMP treatment. However, overall heterogeneity was not significantly different in any of the tested treatments (Figure S4K; Table S3), and non-retinal cell classes tended to be more variable than retinal cell classes (Figures S4J and S4L). Immunolabeling of cryosections of organoids from the same batch used for sci-Plex confirmed the representation of non-retinal cells in these organoids (Figure 4E). Taken together, this suggested that the early modulation of signaling pathways established durable shifts in retinal cell-class representation.

Lastly, we compared the sci-Plex cell counts to measurements of organoid composition obtained by bright-field microscopy. Prior to dissociation, each organoid was imaged in a 96-well plate such that the imaged organoid could be matched to a specific hash barcode. Areas of predicted retina, RPE, and non-retinal tissue were quantified (Figures 4F–4H, S4M, and S4N). Despite differences in the modalities, trends were conserved between the imaging and sci-Plex datasets. Notably, RPE was significantly increased in SU5402:CHIR by both sci-Plex and bright-field microscopy (Figures 4B and 4F). The cell count and area-based measurements from each individual also correlated, although sci-Plex detected a higher retinal composition and the bright-field images detected higher RPE and non-retinal composition (Figure S4O). Overall, we have shown agreement between two highly divergent methods. However, our analysis by bright-field microscopy was limited to a quantification based on broad cell-class domains using 2D images of a 3D object. The ability to quantify all cell classes across hundreds of individual organoids in a manner that agrees with and surpasses the sensitivity and breadth of other methods sets sci-Plex apart as a critical new method for the study of individual organoid cell-class composition.

DISCUSSION

By assaying 410 individual organoids using sci-Plex, we show here that previously intractable analyses are now possible. We identify significant changes in cell-class abundance with a statistically principled methodology. We are also able to, for the first time, comprehensively measure the extensive heterogeneity of retinal organoids, a known but poorly quantified feature of current culturing protocols. Recent publications emphasize the utility of single-cell sequencing to investigate individual organoids and organoid heterogeneity[29,30]; however, no other study has profiled cell-class composition in comparable sample sizes

(E) Immunostaining of cryosectioned day 63 organoids with OTX2 (photoreceptors/RPE/CP, blue), MAP2 (retinal and cortical neurons, green), POU4F2 (RGC, red), and DAPI (gray). Arrow, non-retinal neurons; filled arrowhead, Otx2+ retinal tissue; empty arrowhead, Pou4f2+ retinal tissue. Scale bar represents 100 μm.

(F) Violin plots of percentage of area measurements for RPE as calculated from bright-phase microscopy images of day 62 organoids. Paired t tests followed by Bonferroni correction were used to determine significance ($p < 0.05$). Plots colored as in (C).

(G) Violin plots of size-factor-normalized RPE cell counts for day 63 organoids. Paired t tests followed by Bonferroni correction were used to determine significance ($p < 0.05$). Plots colored as in (C).

(H) Representative bright-field images of day 62 organoids from each group quantified in (F) and (G). Arrow, non-retinal tissue; filled arrowhead, retinal tissue; empty arrowhead, RPE. Scale bar represents 200 μm.

across multiple treatments (32–48 individuals per treatment). Our work represents the most complete investigation of cell-class composition and heterogeneity in any organoid system to date.

Reassuringly, we find that the effect of treatments on cell-class abundance expected from the literature are readily detected. BMP4 treatment increased retinal and lens character in organoids,[18,36,38] Wnt activation in the OV promoted RPE fate determination,[32] and SAG treatment reduced OV cells, reflecting the role of SHH signaling in defining the ventral forebrain.[39,40]

Additionally, our results suggest that retinal organoid protocols might be optimized to generate adjacent neural tissues as well. Tissue that appears non-retinal by bright-field microscopy is routinely dissected away to improve the homogeneity of the cultures. However, when we add a combination of signaling modulators, we generate organoids with optic stalk-like cells, a cell type that is of clinical relevance but for which an established 3D culturing system does not exist.[41] Optic stalk cells would have been discarded as non-retinal by conventional bright-field microscopy; however, they are captured in our study by the unbiased survey of the entire composition of organoids at scale. Further use of the technology in other developmental contexts has the potential to uncover novel culturing systems for additional disease-relevant cell types that may form unexpectedly or that may be difficult to detect by traditional methods.

Another advantage of surveying all cell classes within an organoid, specifically when it can be performed across individuals, is the ability to clarify the sources underlying organoid heterogeneity. We show that it is possible to separate individual organoids into subtypes based on their cell-class composition. With CHIR treatment, >75% of organoids fall into a single subtype defined by high RPC and retinal cell counts, but a secondary subtype defined by high RPE and roof plate content persists. Additional developmental signals that specifically regulate roof plate development could be incorporated in the protocol to reduce heterogeneity.[42]

Lastly, our most surprising result is the CHIR-dependent increase in neural retina at day 28 and the decrease in non-retinal neurons through day 63. Active canonical Wnt signaling is associated with decreased telencephalic identity and increased diencephalic identity, but the role of Wnt in determining the eye field is less well understood.[43,44] Future studies will be needed to determine whether Wnt activation directly promotes the retinal fate or, alternatively, stimulates other non-retinal cells to indirectly drive the retinal identity.

Ultimately, the methodological advancement of sci-Plex and our analytical pipeline facilitates the expansion of perturbation studies in organoids. Sci-Plex can readily be expanded to thousands of individuals across as many conditions as can be cultured. We imagine this will lead to continued improvements to organoid culturing protocols, as well as an expansion in the use of organoids in chemical screening platforms. Although there are many applications for sci-Plex, we envision its utility in the near future to identify ganglion cell survival molecules and to screen for molecules that aid in cone survival as potential treatments for macular degeneration. Outside the retina, this technology holds promise for use with the constantly expanding number of 3D culturing systems.

Limitations of the study

We designed this study in favor of a high number of individual organoids to sample the organoid-to-organoid variation and included only a single organoid culturing technique. Additionally, our analyses focused on cell-class abundances instead of gene expression, namely because the treatments were performed weeks before the organoids were collected. Thus, the effects on gene expression caused at the time of treatment were not captured. Lastly, in our sci-RNA-seq3 hashing experiments, our hash rates were only ~50%. Furthermore, the original sci-RNA-seq3 protocol has a low cell recovery rate, so this protocol is not ideal for rare cell types.

STAR★METHODS

Detailed methods are provided in the online version of this paper and include the following:

- KEY RESOURCES TABLE
- RESOURCE AVAILABILITY
  - Lead contact
  - Materials availability
  - Data and code availability
- EXPERIMENTAL MODEL AND STUDY PARTICIPANT DETAILS
- METHOD DETAILS
  - Stem cell and retinal organoid culture
  - Single cell dissociation
  - Immunostaining
  - Microscopy
  - 10x library preparation
  - Sci-plex (hashing)
  - Sci-RNA-seq
  - Processing of single cell RNA sequencing data
- QUANTIFICATION AND STATISTICAL ANALYSIS
  - Calculation of size factor normalized cell class counts
  - Detection of significant fold changes in cell class abundance
  - Clustering of individual organoids
  - Detection of treatments and cell clusters with high variance

SUPPLEMENTAL INFORMATION

Supplemental information can be found online at https://doi.org/10.1016/j.crmeth.2023.100548.

ACKNOWLEDGMENTS

We thank members of the Trapnell and Reh labs for their comments and discussions. We thank Choli Lee for assistance in flow sorting, the Beliveau lab for use of their Keyence BZ-X810, and the Brotman Baty Institute for support with the data processing pipeline. This work was supported by the NIH (1R01HG010632 to C.T., R01EY021482-12 to T.A.R., and 1F32EY032331 to A.T.); the Paul G. Allen Family Foundation (Allen Discovery Center grant 12357 to C.T.); the CZI (CZF2019-002442 to C.T.); the Foundation Fighting Blindness (TA-RM-0620-0788-UWA to T.A.R.); the Damon Runyon Cancer Research Foundation (DRG-# 32-20 to K.C.E.); and the Hanna H. Gray Fellows Program Award from the HHMI (GT15994 to K.C.E.). Illustrations were created with BioRender.com.

AUTHOR CONTRIBUTIONS

Conceptualization, A.T., A.S., K.C.E., and T.A.R.; methodology, A.T. and C.T.; formal analysis, A.T., K.C.E., and A.S.; investigation, A.T., A.S., K.C.E., D.H., and S.C.; writing – original draft, A.T.; writing – review & editing, A.T., K.C.E., C.T., and T.A.R.; visualization, A.T., A.S., and K.C.E.; supervision, C.T. and T.A.R.; funding acquisition C.T. and T.A.R.

DECLARATION OF INTERESTS

C.T. is a SAB member, consultant, and/or co-founder of Algen Biotechnologies, Altius Therapeutics, and Scale Biosciences. One or more embodiments of one or more patents and patent applications filed by the University of Washington may encompass methods, reagents, and the data disclosed in this manuscript. Some work in this study is related to technology described in patent applications.

Received: December 9, 2022
Revised: May 16, 2023
Accepted: July 14, 2023
Published: August 9, 2023

REFERENCES

1. Eiraku, M., Takata, N., Ishibashi, H., Kawada, M., Sakakura, E., Okuda, S., Sekiguchi, K., Adachi, T., and Sasai, Y. (2011). Self-organizing optic-cup morphogenesis in three-dimensional culture. Nature *472*, 51–56.
2. Nakano, T., Ando, S., Takata, N., Kawada, M., Muguruma, K., Sekiguchi, K., Saito, K., Yonemura, S., Eiraku, M., and Sasai, Y. (2012). Self-formation of optic cups and storable stratified neural retina from human ESCs. Cell Stem Cell *10*, 771–785.
3. Kadoshima, T., Sakaguchi, H., Nakano, T., Soen, M., Ando, S., Eiraku, M., and Sasai, Y. (2013). Self-organization of axial polarity, inside-out layer pattern, and species-specific progenitor dynamics in human ES cell-derived neocortex. Proc. Natl. Acad. Sci. USA *110*, 20284–20289.
4. Lancaster, M.A., Renner, M., Martin, C.-A., Wenzel, D., Bicknell, L.S., Hurles, M.E., Homfray, T., Penninger, J.M., Jackson, A.P., and Knoblich, J.A. (2013). Cerebral organoids model human brain development and microcephaly. Nature *501*, 373–379.
5. Xia, Y., Nivet, E., Sancho-Martinez, I., Gallegos, T., Suzuki, K., Okamura, D., Wu, M.-Z., Dubova, I., Esteban, C.R., Montserrat, N., et al. (2013). Directed differentiation of human pluripotent cells to ureteric bud kidney progenitor-like cells. Nat. Cell Biol. *15*, 1507–1515.
6. Taguchi, A., Kaku, Y., Ohmori, T., Sharmin, S., Ogawa, M., Sasaki, H., and Nishinakamura, R. (2014). Redefining the in vivo origin of metanephric nephron progenitors enables generation of complex kidney structures from pluripotent stem cells. Cell Stem Cell *14*, 53–67.
7. Takasato, M., Er, P.X., Becroft, M., Vanslambrouck, J.M., Stanley, E.G., Elefanty, A.G., and Little, M.H. (2014). Directing human embryonic stem cell differentiation towards a renal lineage generates a self-organizing kidney. Nat. Cell Biol. *16*, 118–126.
8. Fordham, R.P., Yui, S., Hannan, N.R.F., Soendergaard, C., Madgwick, A., Schweiger, P.J., Nielsen, O.H., Vallier, L., Pedersen, R.A., Nakamura, T., et al. (2013). Transplantation of expanded fetal intestinal progenitors contributes to colon regeneration after injury. Cell Stem Cell *13*, 734–744.
9. Hannan, N.R.F., Fordham, R.P., Syed, Y.A., Moignard, V., Berry, A., Bautista, R., Hanley, N.A., Jensen, K.B., and Vallier, L. (2013). Generation of multipotent foregut stem cells from human pluripotent stem cells. Stem Cell Rep. *1*, 293–306.
10. Sridhar, A., Hoshino, A., Finkbeiner, C.R., Chitsazan, A., Dai, L., Haugan, A.K., Eschenbacher, K.M., Jackson, D.L., Trapnell, C., Bermingham-McDonogh, O., et al. (2020). Single-cell transcriptomic comparison of human fetal retina, hPSC-derived retinal organoids, and long-term retinal cultures. Cell Rep. *30*, 1644–1659.e4.
11. Eldred, K.C., Hadyniak, S.E., Hussey, K.A., Brenerman, B., Zhang, P.-W., Chamling, X., Sluch, V.M., Welsbie, D.S., Hattar, S., Taylor, J., et al. (2018). Thyroid hormone signaling specifies cone subtypes in human retinal organoids. Science *362*, eaau6348. https://doi.org/10.1126/science.aau6348.
12. Mayerl, S.J., Bajgai, S., Ludwig, A.L., Jager, L.D., Williams, B.N., Bacig, C., Stoddard, C., Sinha, D., Philpot, B.D., and Gamm, D.M. (2022). Human retinal organoids harboring IMPG2 mutations exhibit a photoreceptor outer segment phenotype that models advanced retinitis pigmentosa. Stem Cell Rep. *17*, 2409–2420.
13. Kallman, A., Capowski, E.E., Wang, J., Kaushik, A.M., Jansen, A.D., Edwards, K.L., Chen, L., Berlinicke, C.A., Joseph Phillips, M., Pierce, E.A., et al. (2020). Investigating cone photoreceptor development using patient-derived NRL null retinal organoids. Commun. Biol. *3*, 82.
14. Aboualizadeh, E., Phillips, M.J., McGregor, J.E., DiLoreto, D.A., Jr., Strazzeri, J.M., Dhakal, K.R., Bateman, B., Jager, L.D., Nilles, K.L., Stuedemann, S.A., et al. (2020). Imaging transplanted photoreceptors in living nonhuman primates with single-cell resolution. Stem Cell Rep. *15*, 482–497.
15. Ripolles-Garcia, A., Dolgova, N., Phillips, M.J., Savina, S., Ludwig, A.L., Stuedemann, S.A., Nlebedum, U., Wolfe, J.H., Garden, O.A., Maminishkis, A., et al. (2022). Systemic immunosuppression promotes survival and integration of subretinally implanted human ESC-derived photoreceptor precursors in dogs. Stem Cell Rep. *17*, 1824–1841.
16. Chao, J.R., Lamba, D.A., Klesert, T.R., Torre, A.L., Hoshino, A., Taylor, R.J., Jayabalu, A., Engel, A.L., Khuu, T.H., Wang, R.K., et al. (2017). Transplantation of human embryonic stem cell-derived retinal cells into the subretinal space of a non-human primate. Transl. Vis. Sci. Technol. *6*, 4.
17. Eldred, K.C., and Reh, T.A. (2021). Human retinal model systems: Strengths, weaknesses, and future directions. Dev. Biol. *480*, 114–122.
18. Fligor, C.M., Huang, K.-C., Lavekar, S.S., VanderWall, K.B., and Meyer, J.S. (2020). Differentiation of retinal organoids from human pluripotent stem cells. Methods Cell Biol. *159*, 279–302.
19. Wagstaff, E.L., Heredero Berzal, A., Boon, C.J.F., Quinn, P.M.J., Ten Asbroek, A.L.M.A., and Bergen, A.A. (2021). The role of small molecules and their effect on the molecular mechanisms of early retinal organoid development. Int. J. Mol. Sci. *22*, 7081. https://doi.org/10.3390/ijms22137081.
20. Cowan, C.S., Renner, M., De Gennaro, M., Gross-Scherf, B., Goldblum, D., Hou, Y., Munz, M., Rodrigues, T.M., Krol, J., Szikra, T., et al. (2020). Cell types of the human retina and its organoids at single-cell resolution. Cell *182*, 1623–1640.e34.
21. O'Hara-Wright, M., and Gonzalez-Cordero, A. (2020). Retinal organoids: a window into human retinal development. Development *147*, dev189746. https://doi.org/10.1242/dev.189746.
22. Lukonin, I., Zinner, M., and Liberali, P. (2021). Organoids in image-based phenotypic chemical screens. Exp. Mol. Med. *53*, 1495–1502.
23. DeStefanis, R.A., Kratz, J.D., Olson, A.M., Sunil, A., DeZeeuw, A.K., Gillette, A.A., Sha, G.C., Johnson, K.A., Pasch, C.A., Clipson, L., et al. (2022). Impact of baseline culture conditions of cancer organoids when determining therapeutic response and tumor heterogeneity. Sci. Rep. *12*, 5205.
24. Renner, H., Grabos, M., Becker, K.J., Kagermeier, T.E., Wu, J., Otto, M., Peischard, S., Zeuschner, D., TsyTsyura, Y., Disse, P., et al. (2020). A fully automated high-throughput workflow for 3D-based chemical screening in human midbrain organoids. Elife *9*, e52904. https://doi.org/10.7554/eLife.52904.
25. Fligor, C.M., Langer, K.B., Sridhar, A., Ren, Y., Shields, P.K., Edler, M.C., Ohlemacher, S.K., Sluch, V.M., Zack, D.J., Zhang, C., et al. (2018). Three-dimensional retinal organoids facilitate the investigation of retinal ganglion cell development, organization and neurite outgrowth from human pluripotent stem cells. Sci. Rep. *8*, 14520.
26. Srivatsan, S.R., McFaline-Figueroa, J.L., Ramani, V., Saunders, L., Cao, J., Packer, J., Pliner, H.A., Jackson, D.L., Daza, R.M., Christiansen, L.,

et al. (2019). Massively multiplex chemical transcriptomics at single cell resolution. Science *6234*, 1–13.

27. Dorrity, M.W., Saunders, L.M., Duran, M., Srivatsan, S.R., Ewing, B., Queitsch, C., Shendure, J., Raible, D.W., Kimelman, D., and Trapnell, C. (2022). Proteostasis governs differential temperature sensitivity across embryonic cell types. Preprint at bioRxiv. https://doi.org/10.1101/2022.08.04.502669.
28. Saunders, L.M., Srivatsan, S.R., Duran, M., Dorrity, M.W., Ewing, B., Linbo, T., Shendure, J., Raible, D.W., Moens, C.B., Kimelman#, D., et al. Deep molecular, cellular and temporal phenotyping of developmental perturbations at whole organism scale. Preprint at bioRxiv. https://doi.org/10.1101/2022.08.04.502764.
29. Uzquiano, A., Kedaigle, A.J., Pigoni, M., Paulsen, B., Adiconis, X., Kim, K., Faits, T., Nagaraja, S., Antón-Bolaños, N., Gerhardinger, C., et al. (2022). Single-cell multiomics atlas of organoid development uncovers longitudinal molecular programs of cellular diversification of the human cerebral cortex. Preprint at bioRxiv. https://doi.org/10.1101/2022.03.17.484798.
30. Bues, J., Biočanin, M., Pezoldt, J., Dainese, R., Chrisnandy, A., Rezakhani, S., Saelens, W., Gardeux, V., Gupta, R., Sarkis, R., et al. (2022). Deterministic scRNA-seq captures variation in intestinal crypt and organoid composition. Nat. Methods *19*, 323–330.
31. Reese, B.E. (2011). Development of the retina and optic pathway. Vis. Res. *51*, 613–632.
32. Fuhrmann, S. (2010). Eye morphogenesis and patterning of the optic vesicle. Curr. Top. Dev. Biol. *93*, 61–84.
33. Diacou, R., Nandigrami, P., Fiser, A., Liu, W., Ashery-Padan, R., and Cvekl, A. (2022). Cell fate decisions, transcription factors and signaling during early retinal development. Prog. Retin. Eye Res. *91*, 101093.
34. Cao, J., Spielmann, M., Qiu, X., Huang, X., Ibrahim, D.M., Hill, A.J., Zhang, F., Mundlos, S., Christiansen, L., Steemers, F.J., et al. (2019). The single-cell transcriptional landscape of mammalian organogenesis. Nature *566*, 496–502.
35. Fujimura, N., Taketo, M.M., Mori, M., Korinek, V., and Kozmik, Z. (2009). Spatial and temporal regulation of Wnt/beta-catenin signaling is essential for development of the retinal pigment epithelium. Dev. Biol. *334*, 31–45.
36. Kuwahara, A., Ozone, C., Nakano, T., Saito, K., Eiraku, M., and Sasai, Y. (2015). Generation of a ciliary margin-like stem cell niche from self-organizing human retinal tissue. Nat. Commun. *6*, 6286.
37. Love, M.I., Huber, W., and Anders, S. (2014). Moderated estimation of fold change and dispersion for RNA-seq data with DESeq2. Genome Biol. *15*, 550.
38. Phillips, M.J., Capowski, E.E., Petersen, A., Jansen, A.D., Barlow, K., Edwards, K.L., and Gamm, D.M. (2018). Generation of a rod-specific NRL reporter line in human pluripotent stem cells. Sci. Rep. *8*, 2370.
39. Chiang, C., Litingtung, Y., Lee, E., Young, K.E., Corden, J.L., Westphal, H., and Beachy, P.A. (1996). Cyclopia and defective axial patterning in mice lacking Sonic hedgehog gene function. Nature *383*, 407–413.
40. Rubenstein, J.L., and Beachy, P.A. (1998). Patterning of the embryonic forebrain. Curr. Opin. Neurobiol. *8*, 18–26.
41. Dutton, G.N. (2004). Congenital disorders of the optic nerve: excavations and hypoplasia. Eye *18*, 1038–1048.
42. Le Dréau, G., and Martí, E. (2012). Dorsal-ventral patterning of the neural tube: a tale of three signals. Dev. Neurobiol. *72*, 1471–1481.
43. Harrison-Uy, S.J., and Pleasure, S.J. (2012). Wnt signaling and forebrain development. Cold Spring Harb. Perspect. Biol. *4*, a008094.
44. Wilson, S.W., and Houart, C. (2004). Early steps in the development of the forebrain. Dev. Cell *6*, 167–181.
45. Cao, J., Packer, J.S., Ramani, V., Cusanovich, D.A., Huynh, C., Daza, R., Qiu, X., Lee, C., Furlan, S.N., Steemers, F.J., et al. (2017). Comprehensive single-cell transcriptional profiling of a multicellular organism. Science *357*, 661–667.
46. Schneider, C.A., Rasband, W.S., and Eliceiri, K.W. (2012). NIH Image to ImageJ: 25 years of image analysis. Nat. Methods *9*, 671–675.
47. Zheng, G.X.Y., Terry, J.M., Belgrader, P., Ryvkin, P., Bent, Z.W., Wilson, R., Ziraldo, S.B., Wheeler, T.D., McDermott, G.P., Zhu, J., et al. (2017). Massively parallel digital transcriptional profiling of single cells. Nat. Commun. *8*, 14049.
48. Stuart, T., Butler, A., Hoffman, P., Hafemeister, C., Papalexi, E., Mauck, W.M., 3rd, Hao, Y., Stoeckius, M., Smibert, P., and Satija, R. (2019). Comprehensive integration of single-cell data. Cell *177*, 1888–1902.e21.
49. Yee, T.W. (2010). The VGAM package for categorical data analysis. J. Stat. Software *32*, 1–34.
50. Hao, Y., Hao, S., Andersen-Nissen, E., Mauck, W.M., 3rd, Zheng, S., Butler, A., Lee, M.J., Wilk, A.J., Darby, C., Zager, M., et al. (2021). Integrated analysis of multimodal single-cell data. Cell *184*, 3573–3587.e29.
51. Butler, A., Hoffman, P., Smibert, P., Papalexi, E., and Satija, R. (2018). Integrating single-cell transcriptomic data across different conditions, technologies, and species. Nat. Biotechnol. *36*, 411–420.
52. Ennis, D.M., and Bi, J. (1998). The beta-binomial model: Accounting for inter-trial variation in replicated difference and preference tests. J. Sens. Stud. *13*, 389–412.
53. Yee, T.W., and Wild, C.J. (1996). Vector generalized additive models. J. R. Stat. Soc. Series B Stat. Methodol. *58*, 481–493.
54. Yee, T.W. (2015). Vector Generalized Linear and Additive Models: With an Implementation in R (Springer).
55. Benjamini, Y., and Hochberg, Y. (1995). Controlling the false discovery rate: a practical and powerful approach to multiple testing. J. R. Stat. Soc. Series B Stat. Methodol. *57*, 289–300.
56. Anders, S., and Huber, W. (2010). Differential expression analysis for sequence count data. Genome Biol. *11*, R106.

STAR★METHODS

KEY RESOURCES TABLE

REAGENT or RESOURCE	SOURCE	IDENTIFIER
Antibodies		
POU4F2	Santa Cruz Biotechnology	Cat# SC-6026; RRID: AB_673441
PAX2	BioLegend	Cat# 901001; RRID: AB_2565001
VSX2	Exalpha Biologicals	Cat# X1180P; RRID: AB_2314191
VSX2	SantaCruz	Cat# Sc-365519; RRID:AB_10842442
MAP2	Sigma-Aldrich	Cat# M9942; RRID:AB_477256
OTX2	Abcam	Cat# ab21990; RRID:AB_776930
ELAVL3/4	Thermo Fisher Scientific	Cat# A-21271; RRID:AB_221448
RCVRN	MIllipore	Cat# AB5585; RRID:AB_2253622
Donkey anti-goat 488 (1:250 dilution)	Thermo Fisher Scientific	Cat# A-11055; RRID:AB_2534102
Donkey anti-rabbit 647 (1:250 dilution)	Thermo Fisher Scientific	Cat# A-31573; RRID:AB_2536183
Donkey anti-sheep 647 (1:300 dilution)	Thermo Fisher Scientific	Cat# A-21448; RRID:AB_2535865
Donkey anti-mouse 488 (1:250 dilution)	Jackson ImmunoResearch Labs	Cat# 715-546-151; RRID:AB_2340850
Donkey anti-mouse 568 (1:250 dilution)	Thermo Fisher Scientific	Cat# A10037; RRID:AB_2534013
Donkey anti-goat 568 (1:250 dilution)	Thermo Fisher Scientific	Cat# A-11057; RRID:AB_2534104
Donkey anti-rabbit 647 (1:250 dilution)	Thermo Fisher Scientific	Cat# A-31573; RRID:AB_2536183
Chemicals, peptides, and recombinant proteins		
Matrigel	Corning	CLS354277
ReLeSR	StemCell Technologies	100–0484
BMP4	R&D Systems	314-BP-050
CHIR99021	Cedarlane Laboratories	04-0004-02
SU5402	Cayman Chemical Co	13182
SAG	Calbiochem	566660
DPBS (no calcium, no magnesium)	ThermoFisher	14190144
Accutase	Sigma	A6964-100ML
FBS	Corning	35-011-CV
Papain and Ovomucoid	Worthington Biochemical	LK003150
Fluromount-G	SouthernBiotech	0100–01
IGEPAL	Sigma-Aldrich	I8896
SuperaseIn RNase Inhibitor	Ambion	AM2694
BSA	NEB	B9000S
5% paraformaldehyde	EMS	50-980-493
Triton X-100	ThermoFisher	A16046.AP
4′,6-diamidino-2-phenylindole (FACS)	Invitrogen	D1306
4′,6-diamidino-2-phenylindole (Immunostaining)	Sigma	D9542
EB buffer	Qiagen	19086
mRNA Second Strand Synthesis buffer	NEB	E6111L
N7 loaded custom TDE1 enzyme	MacroLab, UC Berkeley	N/A
Dimethyl Formamide	Sigma-Aldrich	227056-100ML
DNA binding buffer	Zymo Research	D4004-1-L
D1000 Screen Tape	Agilent Technologies	5067–5583
DNA purification	Zymo Research	D4014
AMPure XP Reagent	Beckman Coulter Life Sciences	A63881

(*Continued on next page*)

Continued

REAGENT or RESOURCE	SOURCE	IDENTIFIER
Critical commercial assays		
Single Cell 3′ v3.1 Dual Index Gene Expression kit (Dual Index Kit TT Set A 96 rxns)	10x Genomics	1000215
Deposited data		
Raw and analyzed data	This paper	GEO: GSE220661
Experimental models: Cell lines		
Human: H9 hESCs *NRL*+/eGFP	Phillips[38]	N/A
Oligonucleotides		
Hashing oligo: 5′-GTCTCGTGGGCTCGGAGATG TGTATAAGAGACAG-[10bp-barcode]-BAAAAAA AAAAAAAAAAAAAAAAAAAAAAAAA-3′ where B is G, C or T	Srivatsan et al.[26]	N/A
Indexed 2-level RT oligo: oligo-dT primer 5'-ACGA CGCTCTTCCGATCTNNNNNNNN-[10bp index]-TT TTTTTTTTTTTTTTTTTTTTTTTTTTTTVN-3', where N is any base and V is either A, C or G	Cao et al.[45]	N/A
Indexed 3-level RT oligo: (5'-[PHO]- CAGAGCNNN NNNNN-[10-bp barcode]-TTTTTTTTTTTTTTTTT TTTTTTTTTT-3′ where N is any base	Cao et al.[34]	N/A
Indexed 3-level ligation oligo: 5′-GCTCTG-[9-bp or 10-bp barcode A]-/dideoxyU/ACGACGCTCTT CCGATCT-[reverse complement of barcode A]-3′	Cao et al.[34]	N/A
Indexed P5 PCR oligo: 5′-AATGATACGGCGACC ACCGAGATCTACAC-[i5]-ACACTCTTTCCCTACA CGACGCTCTTCCGATCT-3′	Cao et al.[45]	N/A
Indexed P7 PCR oligo: 5′-CAAGCAGAAGACGGC ATACGAGAT-[i7]-GTCTCGTGGGCTCGG-3′	Cao et al.[45]	N/A
Software and algorithms		
ImageJ	Schneider et al.[46]	https://imagej.nih.gov/ij/
10x Genomics Cell Ranger	Zheng et al.[47]	https://support.10xgenomics.com/single-cell-gene-expression/software/downloads/latest
Monocle3	Cao et al.[34]	https://cole-trapnell-lab.github.io/monocle3/
BBI pipeline is available at the bbi-lab github page under the bbi-dmux and bbi-sci repositories	NA	https://github.com/bbi-lab
Seurat	Stuart et al.[48]	https://satijalab.org/seurat/
VGAM	Yee[49]	https://CRAN.R-project.org/package=VGAM
Code related to this paper	This paper	https://zenodo.org/badge/latestdoi/654269063
Other		
Keyence BZ-X810 microscope	Keyence	N/A
Zeiss Axio Observer D1	Zeiss	N/A
Zeiss LSM 990	Zeiss	N/A
1.5 mL LoBind microcentrifuge tube	Eppendorf	Z666491
twin.tec™ 96 Well LoBind PCR Plates	Eppendorf	0030129512
Bioruptor Plus	diagenode	B01020001

RESOURCE AVAILABILITY

Lead contact

Further information and requests for resources and reagents should be directed to and will be fulfilled by the lead contact, Thomas A. Reh (tomreh@uw.edu).

Materials availability

No unique materials were generated by this study.

Data and code availability

- Single-cell RNA-seq data have been deposited at GEO and are publicly available at GEO: GSE220661. The accession number is also listed in the key resources table. Microscopy data reported in this paper will be shared by the lead contact upon request.
- All original code has been deposited at Zenodo: https://doi.org/10.5281/zenodo.8088246 and is publicly available as of the date of publication. DOIs are listed in the key resources table.
- Any additional information required to reanalyze the data reported in this paper is available from the lead contact upon request.

EXPERIMENTAL MODEL AND STUDY PARTICIPANT DETAILS

The parent cell line used for all experiments was the female human embryonic stem cell line (hESC) H9 (WiCell, Madison, WI, https://www.wicell.org). H9 hESCs contain an *NRL*$^{+/eGFP}$ reporter[38] contain. All organoids of the same age were from the same batch, but each age was from a different starting batch of organoids. The time matched sci-Plex and immunostaining experiments used organoids from the same batch.

Experiment	Age	Line	Organoids Used
10x match	D78	H9	5 pooled
10x match	D185	H9	5 pooled
10x match	D29	H9	10 pooled
D28	D28	H9	314 individuals
D63	D63	H9	96 individuals

METHOD DETAILS

Stem cell and retinal organoid culture

hESCs were maintained by dissociation and propagation in StemFlex media (ThermoFisher, A3349401) on Matrigel (Corning, CLS354277) coated plates at 37°C in 5% CO_2. hESC colonies were passaged by dissociation with ReLeSR (StemCell Technologies, 100–0484). Retinal organoids were grown as described in[18] with minor alterations mentioned herein. The cell culture medias used were Neural induction media, or NIM: 484.5mL DMEM/F12 (Life Technologies, Catalog #11330-057), 5mL N2 supplement (Life Technologies, Catalog #17502048), 5mL MEM NEAA (Life Technologies, Catalog# 11140050), 5mL penicillin-streptomycin (Life Technologies, Catalog# 15240062). Retinal differentiation media, or RDM: 240mL DMEM/F12 (Life Technologies, Catalog #11330-057), 240mL DMEM (Life Technologies, Catalog #12430062), 10mL B27 supplement (Life Technologies, Catalog #17504001), 5mL MEM NEAA (Life Technologies, Catalog #11140050), 5mL penicillin-streptomycin (Life Technologies, Catalog #15240062) + 1%, 3%, or 5% FBS (Corning, Catalog #35-011-CV) based on protocol needs.

In brief, confluent stem cell colonies were lifted from the plate using dispase (2 mg/mL, Life Technologies, Catalog #17105041) for 5–10 min, then forcefully removed by pipetting 2 mL/well of DMEM (Life Technologies, Catalog #12430062) directly onto cells using a 1 mL pipette. Colonies were removed from the 6 well plates and allowed to settle to the bottom of a 15 mL collection tube by gravity. The supernatant was removed, and colonies were transferred to a T25 tissue culture flask in a 3:1 StemFlex:NIM mix for a total of 10 mL per flask. Full media change was performed the following day (Day 1) with 10 mL of 1:2 StemFlex:NIM. Day 2 a full media change was performed and replaced with 10 mL of NIM. Day 3 a full media change was performed and replaced with 10 mL of NIM. Day 5 a full media change was performed and replaced with 10 mL of NIM. Day 7 a full media change was performed and replaced with 10 mL of NIM, and BMP4 BMP4 (1.5 nM, R&D Systems, 314-BP-050) was added to the media to a final concentration of 1.5nM. Day 8 EBs were then evenly distributed between the 6 wells of a 6 well plate. The media was not changed, and EBs were moved and cultured in the BMP4 containing NIM media they were in. 200 μL of FBS was added to allow for EBs to stick to the bottom of the plate. Days 10–20, every other day, a full media change was performed with fresh NIM. Days 14 and 16 a full media change was performed with NIM, and the signaling factor modulators CHIR99021 (3 μM, Cedarlane Laboratories, 04-0004-02), SU5402 (1 μM, Cayman Chemical Co, 13182), and/or SAG (1 μM, Calbiochem, 566660) were added depending on the treatment group. For the None treatment, DMSO was added at the same volume and time in which SU5402 was added. EBs were then manually lifted from the plates on day 20 or 21 by forcefully pipetting 2 mL/well of DMEM directly onto EBs using a 1 mL pipette. EBs were removed from the 6 well plates and allowed to settle to the bottom of a 15 mL collection tube by gravity. From this point on we consider the cells retinal organoids. The supernatant was removed, then organoids were resuspended in RDM with 1% FBS. Two days later media was

exchanged with RDM +3% FBS, and two days after that with RDM +5% FBS. From this point on, cells were maintained with a full media change of RDM +5% FBS every two to three days.

Single cell dissociation

Organoids were placed into 96-well v-bottom plates. For the 10x comparison, 5–10 organoids were added to each well. In the D28 and D63 experiments, a single organoid was added to each well. Media was removed, the organoids were washed in DPBS (no calcium, no magnesium) (ThermoFisher, 14190144). For the D28 and D63 organoids, 100 μL of accutase (Sigma, A6964-100ML) was added to the cultures. The cultures were incubated at 37°C on a nutator for 15 min. After 15 min, organoids were pipetted up and down as needed (every 5–10 min). The extent of dissociation was determined by bright-field microscopy. When clusters of cells could no longer be seen, the accutase was deactivated by the addition of 20 μl of FBS (Corning, 35-011-CV). This was done on an organoid-by-organoid basis as some dissociate faster than others. The dissociation was complete by 30–45 min after accutase addition. For the D78 and D185 organoids, the dissociation was performed with 100 μL of papain (Worthington Biochemical, LK003150). The dissociation was performed as above and was completed within 15–20 min. 100 μL of Ovomucoid (Worthington Biochemical, LK003150) was used to deactivate the reaction. After deactivation of accutase or papain cells were spun down at 700 g for 3 min, then resuspended in a single cell suspension in RDM media[18] for sci-Plex processing.

Immunostaining

Organoids were fixed in 4% paraformaldehyde, 5% sucrose for 30–45 min followed by 3 washes in 1X PBS. All samples were then transitioned into 10%, then 20% and then 30% solutions of sucrose for at least 30 min each solution. Organoids were then embedded in OCT and cryosectioned at 14–16 mm. For immunostaining, slides were washed three times in 1X PBS, then blocked in blocking buffer (0.5%Triton and 10% horse serum) for 20–60 min, followed by addition of primary antibody diluted in blocking buffer and incubation at 4C overnight. The following day, slides were washed 3 times in 1X PBS, then the appropriate 488/568/647 fluorophore-conjugated secondary antibody, diluted in blocking buffer, was added and incubated for 1 h at room temperature. Slides were mounted using Fluromount-G (SouthernBiotech, 0100-01). Details of the antibodies used in this study are provided below. For the D28 organoids, between 3 and 7 organoids were stained per condition (All = 5, BMP = 3, CHIR = 5, None = 5, SAG = 7, SU5402 = 5, SU5402:CHIR = 5).

Antibody	Source	Catalog #	Dilution
POU4F2	Santa Cruz Biotechnology	SC-6026	1:300
PAX2	BioLegend	901001	1:300
VSX2	Exalpha Biologicals	X1180P	1:300
VSX2	SantaCruz	Sc-365519	1:300
MAP2	Sigma	M9942	1:200
OTX2	ABCAM	21990	1:300
ELAVL3/4	Invitrogen	A-21271	1:100
RCVRN	Chemicon	AB5585	1:200

Microscopy

For brightfield images, single organoids were placed into each well of a round-bottom 96-well plate and imaged at 4x magnification with a Keyence BZ-×810 microscope. Group bright-field images were obtained at 4x magnification using the Zeiss Axio Observer D1. Confocal images were obtained using the Zeiss LSM 990. Image processing was done in ImageJ.[46] Area measurements were obtained by setting a standardized threshold per channel.

10x library preparation

Dissociated cells were subjected to the standard 10x workflow for Single Cell 3′ v3.1 Dual Index Gene Expression kit (Dual Index Kit TT Set A 96 rxns, 10x Genomics, 1000215).

Sci-plex (hashing)

Hashing of organoids uses a protocol adapted from the original sci-Plex publication.[26] Single-cell suspensions in 96-well v-bottom plates were centrifuged at 600 x g for 5 min. This step and all following centrifugation steps were performed in a swinging bucket centrifuge that was chilled to 4°C. Media was removed by aspiration. Cells were washed with 200 μL 1 x dPBS (no calcium, no magnesium) in each well. After centrifugation of the v-bottom plate, the dPBS was removed from wells by aspiration, and 50 μL of CLB+hash solution (45 μL of Cold Lysis Buffer – 10mM Tris/HCl pH 7.4, 10mM NaCl, 3mM MgCl2, 0.1% IGEPAL, 1% (v/v, Sigma-Aldrich, I8896), SuperaseIn RNase Inhibitor (20 U/μL, Ambion, AM2694), 1% (v/v) BSA (20 mg/mL, NEB, B9000S) + 5μL of

hash oligo (10 μM, IDT)) was added to the well. The cells were mixed with the CLB+hash by pipetting up and down for 5–10 strokes. The plate was allowed to sit on ice for 3 min. To fix the hashes to the nuclei, 200 μL of fixation buffer (5% paraformaldehyde (EMS, cat. no. 50-980-493), 1.25x dPBS) was mixed with the nuclei by pipetting up and down for 10 strokes. The nuclei were fixed on ice for 15 min and then all wells of a plate were pooled into a single 50 mL conical tube. The hashed nuclei were centrifuged for 5 min at 800xg. Pellets were resuspended in 1mL of NSB (Nuclei Buffer + SuperaseIn + BSA – 10mM Tris/HCl pH 7.4, 10mM NaCl, 3mM MgCl2, 1% (v/v) BSA, 1% (v/v) SuperaseIn RNase Inhibitor) and all 50 mL tubes were pooled into a single 50 mL conical. Nuclei were centrifuged for 5 min at 800 x g and resuspended again in 1 mL of cold NSB. Nuclei were transferred to a 1.5 mL LoBind microcentrifuge tube (Eppendorf, Z666491). The number of nuclei recovered was counted using a hemocytometer. In order to continue centrifuging in a swinging bucket centrifuge, the 1.5 mL tube was placed within a 15 mL conical. The nuclei were centrifuged one final time for 5 min at 800 x g and they were resuspended in 500 μL of NSB. Samples were flash frozen in liquid nitrogen and stored at −80C.

Sci-RNA-seq

The sci-RNA-seq experiment described in Figure 1 was prepared by the original sci-RNA-seq protocol[45] with minor modifications. Briefly, fixed nuclei were thawed and centrifuged at 800 x g for 5 min. Nuclei were permeabilized with 500 μL NSB +0.2% Triton X-100 (ThermoFisher, A16046.AP) on ice for 3 min. Nuclei were centrifuged for 10 min at 800 x g and resuspended in 400 μL NSB. A final centrifugation step was performed at 800 x g for 10 min. The nuclei were diluted to ∼300 nuclei per uL across 2 x twin.tec 96 Well LoBind PCR Plates (Eppendorf, 0030129512). The reverse transcription reaction was set up as in Cao et al., and the RT reaction was carried out using an increasing temperature gradient (4°C 2 min, 10°C 2 min, 20°C 2 min, 30°C 2 min, 40°C 2 min, 50°C 2 min, 55°C 15 min) without the addition of any reagents to stop the reaction upon completion. All nuclei were pooled and stained with DAPI (4′,6-diamidino-2-phenylindole, 3 μM final) (Invitrogen, D1306). Using a FACSAria III cell sorter (BD Biosciences), 50 nuclei were sorted into each well of 4 twin.tec 96 Well LoBind PCR Plates that had 5 μL of EB buffer (Qiagen, 19086), 0.5 μL of 5 x mRNA Second Strand Synthesis buffer (New England Biolabs, E6111L), and 0.25 μL of mRNA Second Strand Synthesis enzyme (New England Biolabs, E6111L) in each well. The plates were incubated at 16°C for 3 h. To each well, 5.75 μL of Tagmentation mix (1.1 μL N7 loaded custom TDE1 enzyme (MacroLab, UC Berkeley) per 632.5 μL 2xTD buffer (20 mM Tris-HCl pH 7.6, 10 mM $MgCl_2$, 20% v/v Dimethyl Formamide (Sigma-Aldrich, 227056-100ML)) was added and mixed by pipetting 10 x. Tagmentation was carried out at 55C for 5 min before being stopped by the addition of 12 μL of DNA binding buffer (Zymo Research, D4004-1-L) for 5 min at room temperature. Ampure-based bead purification, PCR, and final library purification was performed as published previously.[45] The library was visualized using a D1000 Screen Tape (Agilent Technologies, 5067–5583).

Both of the individual organoid datasets were prepared following the sci-RNA-seq3 protocol from Srivatsan et al. with modifications noted below. As above, all centrifugation speeds were performed at 800 x g. Fixed nuclei were thawed and centrifuged for 5 min. Nuclei were permeabilized with 500 μL NSB +0.2% Triton X-100 on ice for 3 min. Nuclei were centrifuged for 10 min and resuspended in 400 μL NSB to wash away the Triton. The nuclei were sonicated with a Bioruptor Plus (diagenode) sonication device on low power for 12 s. A final centrifugation step was then performed for 10 min. Nuclei were suspended to a concentration of 1000–2500 nuclei/uL with 22,000–55,000 nuclei added to each well of 2 x twin.tec 96 Well LoBind PCR Plates. From here only minor modifications from the Srivatsan protocol were performed. Of note, before second strand synthesis 2500-3000 nuclei were distributed into each well, during tagmentation the 10 μL of tagmentation mix was composed of 0.05 μL of a custom TDE1 enzyme in 9.95μL of 2 x TD buffer, and when performing the well-based Ampure bead purification the volume of beads was increased to 60 μL per well. PCR was performed for 13 cycles and libraries were purified with column-based DNA purification (Zymo Research, D4014) followed by 0.8x Ampure bead cleanup. Libraries were visualized using D1000 or HS D1000 Screen Tapes.

In-depth protocols can be found on protocols.io under the following titles.

2-level: Single cell RNA sequencing library preparation (2-level sci-RNA-seq)

3-level: sci-RNA-seq3.

Processing of single cell RNA sequencing data

10x

The 10x libraries from D28, D78, and D185 organoids were sequenced on an Illumina NextSeq 2000 and a NextSeq 550 (Read 1: 28, Index 1: 10, Index 2: 10, Read 2: 75) and processed by CellRanger (3.1.0)[47] using the default settings. The output was imported into Monocle3 (1.0.0),[34] and data from the three runs were combined into a single object with the corresponding sci-Plex dataset.

Sci-Plex (10x comparison)

The sci-Plex library was sequenced on an Illumina Nextseq550 (High Output 75 cycle kit) with 18 cycles for Read1, 10 cycles for each index, and 52 cycles for Read2. The reads were processed using a pipeline developed by the Brotman Baty Institute (BBI). This BBI pipeline is available at the bbi-lab github page under the bbi-dmux and bbi-sci repositories (https://github.com/bbi-lab). The output was imported into Monocle3, and custom code (https://github.com/atresen/individual_retinal_organoids) was used to incorporate the hash information outputted by the pipeline into the Monocle3 cds object. Cells with fewer than 1000 UMIs and >20,000 UMIs were discarded. Hashing success was determined by the ratio of the most prevalent hash barcode for a cell compared to the second most prevalent hash barcode. If the top_to_second_best_ratio was >3 the cell was considered hashed. All cells below that cutoff were discarded. The filtered sci-Plex data was combined with the 10x data. The combined object was converted into a Seurat object

for CCA integration following the "Introduction to scRNA-seq integration" vignette.[48,50,51] The integration anchors were found using 100 dimensions and 100 anchor features. A 3D UMAP was constructed from 50 PCA dimensions with a mindist of 0.2 and 50 nearest neighbors. The UMAP coordinates outputted from the integration were transferred back to Monocle3 from which the remainder of the analysis and plotting was performed. Clusters were determined using cluster_cells() in Monocle3 using the default assigned resolution. Common marker genes for retinal cell classes compiled from previous single cell and bulk transcriptomic studies of retinal development in fetal human (from our group and others) were then plotted on to the UMAP to determine the clusters with which they were most associated (Table S2). For some clusters, common retinal markers were not sufficient to assign cell classes. In those cases, genes with high specificity to that cluster were determined using custom code (https://github.com/atresen/individual_retinal_organoids). These genes were then used to aid in a cell class determination (Table S2).

Sci-Plex (D28 individual organoids)

The sci-Plex library was sequenced on an Illumina NextSeq 2000 (P2 100 cycle kit) with 35 cycles for Read 1, 10 cycles for each index, and 70 cycles for Read2. Reads were processed using the BBI pipeline as described above. The output was imported into Monocle3. A preliminary filtering was performed for cells with >100 UMIs, less than 20,000 UMIs, and <15% mitochondrial reads. Cells with a top_to_second_best_ratio <3 were also removed from the analysis. Size factors were estimated, the data was preprocessed with 40 PCA dimensions, correction was performed to account for the number of UMIs per cell. UMAPs were projected in 2 dimensions with a mindist of 0.1 and 15 nearest neighbors. Cells were clustered with a resolution of 5×10^{-5}. cell classes were assigned using well-established marker genes (Table S2). For the analysis of individual organoids, only organoids with at least 50 cells were used.

Sci-Plex (D63 individual organoids)

The sci-Plex library was sequenced on a Nextseq 2000 (P2 100 cycle kit) with 35 cycles for Read 1, 10 cycles for each index, and 70 cycles for Read2. Reads were processed using the BBI pipeline as described above. The output was imported into Monocle3. A preliminary filtering was performed for cells with >150 UMIs, less than 20,000 UMIs, and <15% mitochondrial reads. Cells with a top_to_second_best_ratio <2.5 were also removed from the analysis. Size factors were estimated, the data was preprocessed with 30 PCA dimensions, correction was performed to account for the number of UMIs per cell. UMAPs were projected in 2 dimensions with a mindist of 0.1 and 50 nearest neighbors. Cells were clustered with a resolution of 5×10^{-5}. cell classes were assigned using well-established marker genes (Table S2). Only organoids with at least 50 cells were used in downstream analyses.

QUANTIFICATION AND STATISTICAL ANALYSIS

Calculation of size factor normalized cell class counts

Size factor normalized cell counts were calculated as in.[27,28] Briefly, counts for cells of the same cell class within each organoid were added up and organized into a cell class by organoid matrix. A Monocle3 cds was created from the matrix, and `size factors()`, which takes the total number of cells in the organoid and divides it by the geometric mean of cell counts for all organoids, was run. The number of cells of each cell class in each organoid was divided by the size factor of that organoid. All values were rounded to the nearest whole number.

Detection of significant fold changes in cell class abundance

A generalized linear model was fit to the normalized data using a beta-binomial distribution[52] as in.[27,28]

$$logit(\mu_i) = \beta_t x_t + \beta_0$$

$$logit(p_i) = X_t x_t + X_0$$

$$y_i = BeBin(\mu_i, p_i)$$

where y_i represents the normalized cell count distribution for cell class i, μ_i is the mean of the distribution, and ρ_i is the overdispersion or "litter effect" associated with the beta-binomial distribution. The binary indicator.

variable X_t denotes which treatment the organoids were exposed to. All D28 treatments were first modeled with respect to the None treatment. The CHIR, SU5402, and SU5402:CHIR treatments were later modeled compared to the BMP treatment. At D63 CHIR and SU5402:CHIR treatments were modeled compared to BMP. The models were fit using the VGAM package, and p values were determined by a Wald test on β_t.[53,54] Abundance changes were determined significant if the q-value after Benjamini Hochberg correction was < 0.05.[55] In D28 organoids, the model above was also used to determine significant abundances changes in specific retinal cell populations. When this was performed, all cell classes were included in the calculation even though only the retinal cell classes are displayed in the heatmap in Figure S3D.

Clustering of individual organoids

Counts for cells of the same cell class within each organoid were added up and organized into a cell class by organoid matrix. A Monocle3 cds was created from the matrix and `size factors()` was run. The cds was processed `preprocess_cds(cds, method = ''PCA'', norm_method = ''size_only'', num_dim = 9)` and then subjected to dimensionality reduction in two dimensions by UMAP `reduce_dimension(cds, umap.n_neighbors = 30, umap.min_dist = 0.05)`. Clustering was performed with a resolution of 1×10^{-2}.

Detection of treatments and cell clusters with high variance

A cluster by individual organoid matrix was calculated, size factors were determined, and a generalized linear model was fit to the normalized data using a beta-binomial distribution as above. The VGAM package doesn't automatically model dispersions for the beta-binomial distribution, so `simulate.vlm()` was run 100 times to model the mean and standard deviation which was then used to calculate the coefficient of variation ($CV = \sigma/\mu$) for each cluster and each treatment (i.e., the normalized cell counts for the 48 organoids exposed to CHIR treatment were determined for cluster 1 and then the mean and variance were calculated. This was repeated for each of the treatments and then each of the clusters). Because variance scales with the mean, the coefficient of variation (CV) was calculated by taking the ratio of the standard deviation over the mean as a means to normalize the amount of variance such that we can compare the variance in clusters with high cell counts to clusters with low cells counts. As randomness is increased at smaller values, we expect that clusters with fewer cells will have higher CV and clusters with more cells will have lower CV values. A gamma-valued glm of the form pioneered by DESeq[56] was then to capture the trend between the average number of cells in a cluster across organoids and that cluster's CV using VGAM.[53,54] To identify clusters with higher than expected CV, conditional upon treatment, we tested whether the CV for a given cluster exceeded this model's 95% confidence interval's upper limit.

To assess whether a treatment altered heterogeneity compared to the BMP treatment, a likelihood-ratio test was used to compare the output of the gamma distribution to a reduced model that excludes the treatment term. Treatments were considered more heterogeneous than BMP if the likelihood-ratio test produced a q-value after Benjamini Hochberg correction of <0.05 indicating that use of `treatment` as a factor improves the model and the sign of the treatment term was positive indicating that the treatment-dependent change led to an increase in heterogeneity.[55]

Cell Reports Methods, Volume *3*

Supplemental information

Single-cell sequencing of individual retinal organoids reveals determinants of cell-fate heterogeneity

Amy Tresenrider, Akshayalakshmi Sridhar, Kiara C. Eldred, Sophia Cuschieri, Dawn Hoffer, Cole Trapnell, and Thomas A. Reh

Supplemental Information

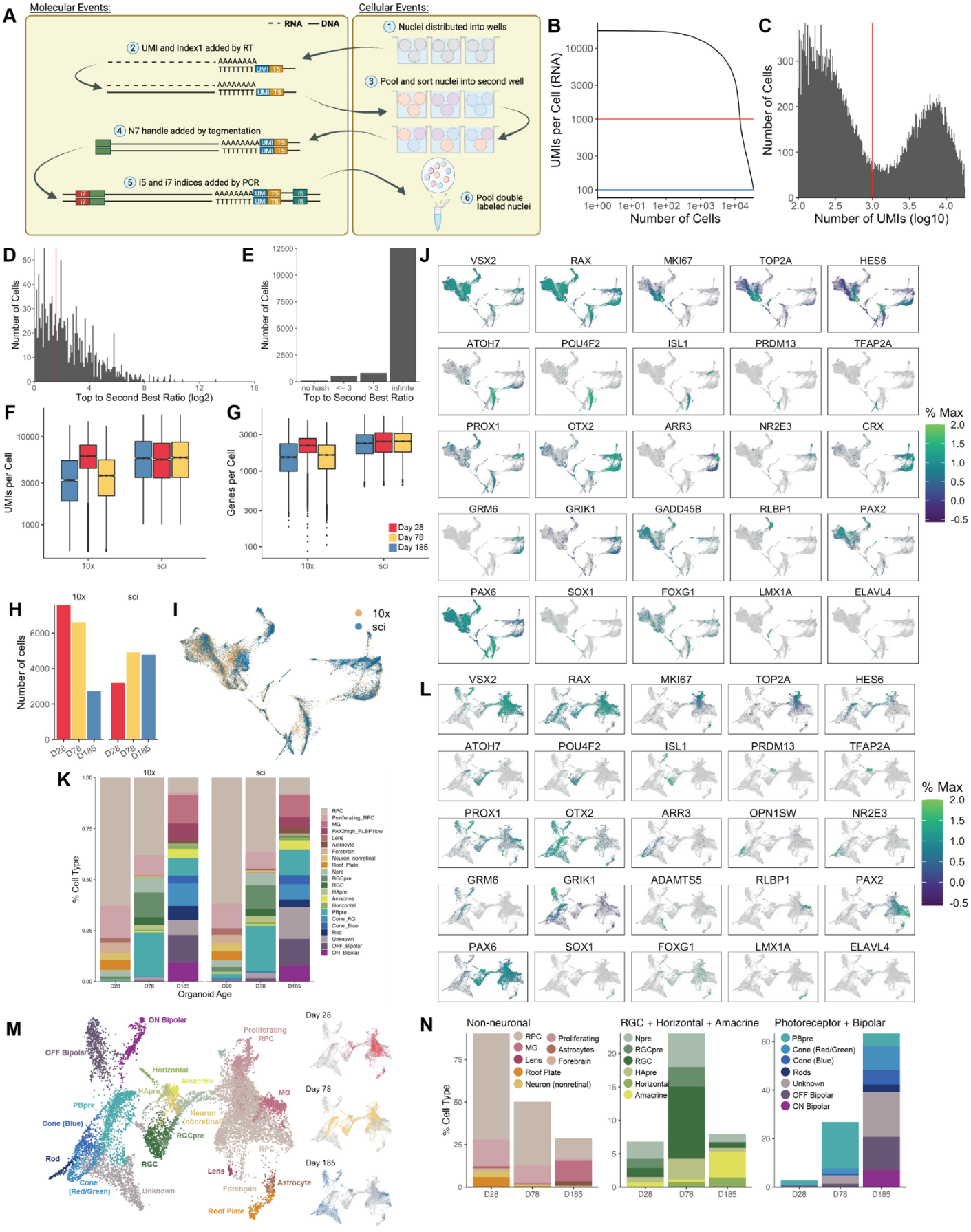
A
Molecular Events:
Cellular Events:
RNA
DNA
1 Nuclei distributed into wells
2 UMI and Index1 added by RT
3 Pool and sort nuclei into second well
4 N7 handle added by tagmentation
5 i5 and i7 indices added by PCR
6 Pool double labeled nuclei
B
UMIs per Cell (RNA)
Number of Cells
C
Number of Cells
Number of UMIs (log10)
D
Number of Cells
Top to Second Best Ratio (log2)
E
Number of Cells
no hash
<= 3
> 3
infinite
Top to Second Best Ratio
F
UMIs per Cell
10x
sci
G
Genes per Cell
Day 28
Day 78
Day 185
H
Number of cells
D28
D78
D185
I
10x
sci
J
VSX2
RAX
MKI67
TOP2A
HES6
ATOH7
POU4F2
ISL1
PRDM13
TFAP2A
PROX1
OTX2
ARR3
NR2E3
CRX
GRM6
GRIK1
GADD45B
RLBP1
PAX2
PAX6
SOX1
FOXG1
LMX1A
ELAVL4
% Max
K
% Cell Type
Organoid Age
RPC
Proliferating_RPC
MG
PAX2high_RLBP1low
Lens
Astrocyte
Forebrain
Neuron_nonretinal
Roof_Plate
Npre
RGCpre
RGC
HApre
Amacrine
Horizontal
PBpre
Cone_RG
Cone_Blue
Rod
Unknown
OFF_Bipolar
ON_Bipolar
L
ADAMTS5
OPN1SW
M
ON Bipolar
OFF Bipolar
Proliferating RPC
Horizontal
Amacrine
HApre
PBpre
Cone (Blue)
Neuron (nonretinal)
RGCpre
MG
Rod
RGC
Cone (Red/Green)
Unknown
Lens
Forebrain
Astrocyte
Roof Plate
Day 28
Day 78
Day 185
N
Non-neuronal
RGC + Horizontal + Amacrine
Photoreceptor + Bipolar
RPC
MG
Lens
Roof Plate
Neuron (nonretinal)
Proliferating
Astrocytes
Forebrain
Npre
RGCpre
RGC
HApre
Horizontal
Amacrine
PBpre
Cone (Red/Green)
Cone (Blue)
Rods
Unknown
OFF Bipolar
ON Bipolar
% Cell Type
D28
D78
D185

Figure S1. Quality control of sci-Plex and 10x comparison datasets, related to Figure 1. A) sci-RNA-seq relies on successive split-pool barcoding of RNA: permeabilized nuclei are distributed into wells of a 96-well plate. Reverse transcription is performed using a polyD-T oligo that contains both a UMI and barcode (T5). Each well is provided a unique oligo such that all cDNA molecules produced in a well will have the same barcode. Cells are then pooled and redistributed into a second set of 96-well plates. The cDNA is converted to dsDNA and subjected to tagmentation which adds a uniform sequence to the end of the cDNA molecules. This sequence and the sequence at the end of the RT oligos can be used to amplify the library by PCR. The PCR primers each contain barcode sequences (i7, i5) and the wells all receive a unique combination of PCR oligos. Experiments can be designed such that the vast majority of cells travel through a unique set of wells. Thus, RNAs that share the same barcode combination are assumed to have come from the same cell. **B)** A knee plot of the number of UMIs per cell compared to the number of cells recovered. The red line (1000UMIs) indicates the value denoting whether a barcode combination should be considered a cell. **C)** A histogram of the number of cells per UMI count. UMI counts left of the red line (1000 UMIs) are removed from the analysis. **D)** Hashes were sequenced and assigned to cells. A Top to Second Best Ratio was then calculated by dividing the UMI count of the most common hash barcode by the UMI count of the second most common hash barcode detected for an individual cell. A histogram of the number of cells recovered at each Top to Second Best Ratio was then generated. The red line (3) denotes the Top to Second Best Ratio required for a cell to be assigned a confident hash call. **E)** A bar plot of the number of cells with Top to Second Best Ratios matching given criteria. In the event only a single hash barcode is detected, the ratio is infinite. **F)** Bar plots of the number of cells recovered for each sample. **G)** Box plots of the number of UMIs recovered from each cell for each sample. **H)** Box plots of the number of genes recovered from each cell for each sample. **I)** Integration of 10x and sci data by Seurat's MNN-CCA methodology. The cells are colored by the technology with which they were prepared for sequencing. **J)** Feature plots of the genes used to define cell types from the integrated sci-Plex and 10x UMAP. **K)** Stacked bar plots demonstrating the cell type compositions of organoids from D28, D78, and D185 organoids as prepared for sequencing by 10x and sci-Plex. RPC: retinal progenitor cell, MG: Müller glia, Npre: retinal neuronal precursor, RGC: retinal ganglion cell, RGCpre: RGC precursor, HApre: horizontal/amacrine precursor, PBpre: photoreceptor/bipolar precursor, Cone_RG: red/green cone. **L)** A UMAP was generated by Monocle3 using only the cells recovered by sci-Plex. Cells are colored by expression of the indicated gene. The displayed genes were used when defining cell types. **M)** The UMAP from L). Left: Cells are colored by cell type, Right: Cells are faceted and colored by organoid age. **N)** Using the cell type assignments from M, cell types were split into Brain/Non-neuronal (Non-neuronal), RGC+Horizontal+Amacrine (RGC+H+A), and Photoreceptor+Bipolar (PR+BP) categories. Cells were counted and the % Cell Type was determined for each organoid age.

—----------

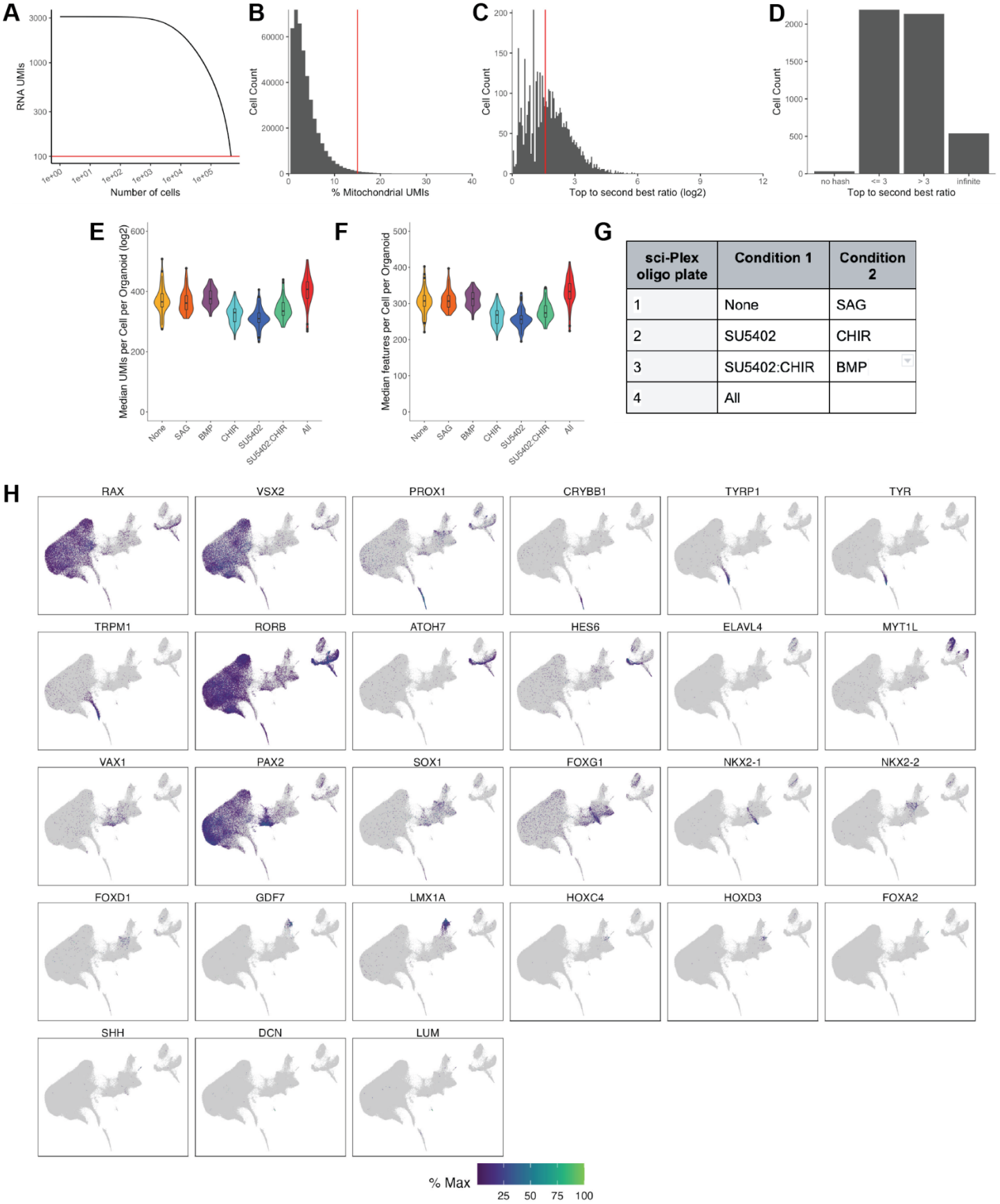

sci-Plex oligo plate	Condition 1	Condition 2
1	None	SAG
2	SU5402	CHIR
3	SU5402:CHIR	BMP
4	All	

Figure S2. Quality control of sci-Plex performed on individual D28 organoids, related to Figure 2. A) A knee plot of the number of UMIs per cell compared to the number of cells recovered from D28 organoids. The red line (100 UMIs) indicates the value denoting whether a barcode combination should be considered a cell. **B)** A histogram of the % mitochondrial UMIs. Cells with percentages right of the red line (15%) are removed from the analysis. **C)** A histogram of the number of cells recovered at each Top to Second Best Ratio was then generated. The red line (2.5) denotes the Top to Second Best Ratio required for a cell to be assigned a confident hash call. In the event only a single hash barcode is detected, the ratio is infinite. **D)** A bar plot of the number of cells with Top to Second Best Ratios matching given criteria. **E)** Violin plots of the number of UMIs recovered from each cell for each D28 organoid per treatment. **F)** Violin plots of the number of features recovered from each cell for each D28 organoid per treatment. **G)** Table indicating which sci-Plex oligo plate was used to hash each of the treatment conditions. **H)**Expression plots of the genes used to define the cell types in Figure 2E.

—----------

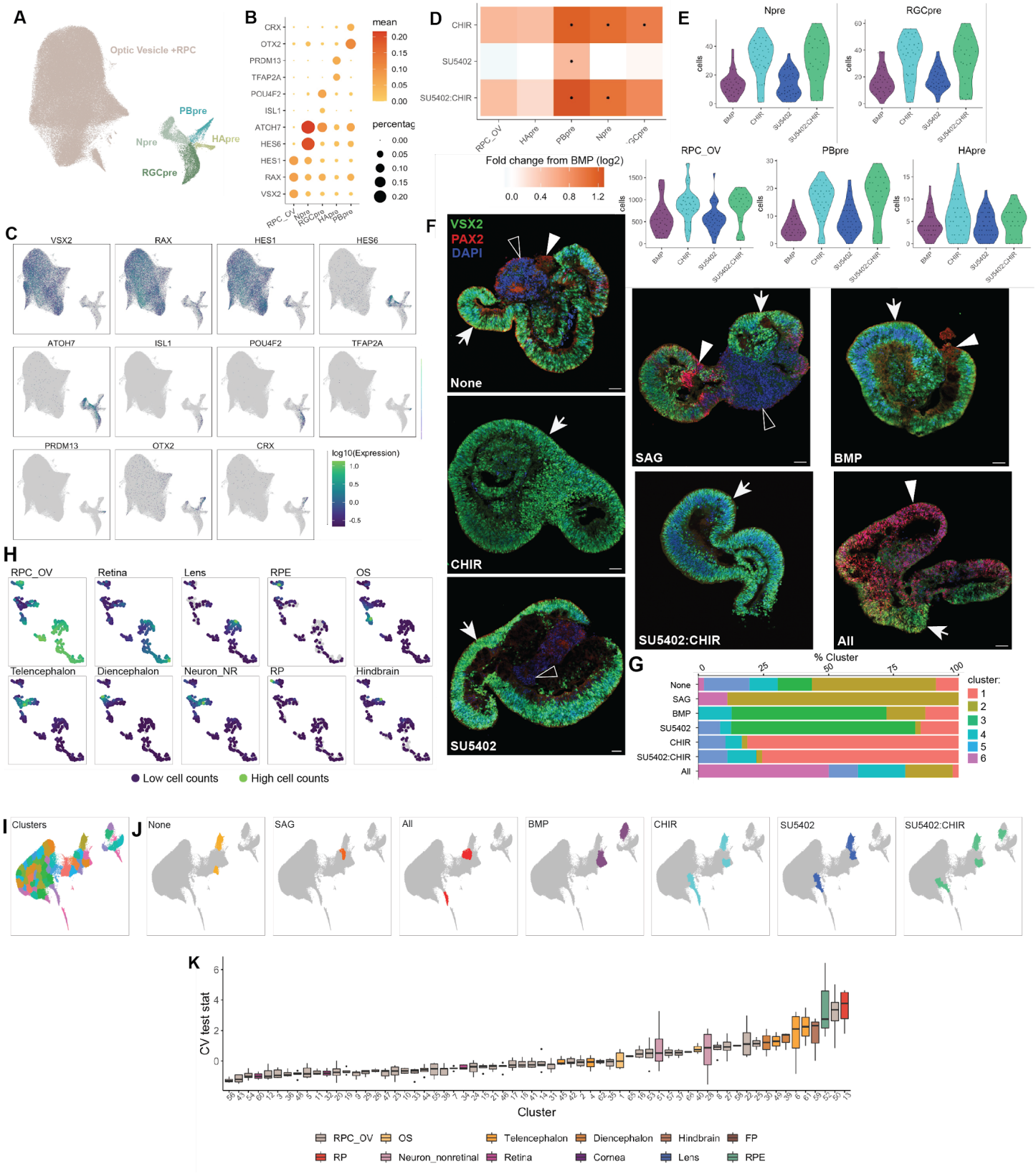

Figure S3. Investigation of abundance changes in specific retinal cell types and cell types with high variability, related to Figure 3. A) A UMAP of the Retina and RPC_OV subset of cells from D28 organoids was derived by Monocle3. Cells are colored by retinal cell type. RPC_OV: retinal progenitor cell/optic vesicle,

Npre: retinal neuronal precursor, RGCpre: retinal ganglion cell precursor, HApre: horizontal/amacrine precursor, PBpre: photoreceptor/bipolar precursor. **B)** A dot plot of the genes used to identify the retinal cell types in A. **C)** Expression plots of the genes used to define the cell types in Figure S4A. **D)** Heatmap of fold change in cell type abundance compared to “BMP” for D28 organoids. A beta-binomial model was fit to the data and used to determine whether there were significant changes in cell type abundances. A * in the center of the box indicates a q-value of less than 0.05 after Benjamini Hochberg correction. Note that while only the retinal cell types are displayed, the test was performed on size-factor normalized cell counts of all cell types in the organoid. **E)** Violin plots of size-factor normalized cell counts for the retinal cell types. Plots are colored by treatment. **F)** Immunostaining of D28 organoids with VSX2 (RPCs/Npre, green), PAX2 (OS, red), and DAPI (blue). Scale bar represents 50 μm. Arrow = RPCs/Npre, empty arrow head = non-optic-stalk (OS), filled arrow head = OS. **G)** Stacked bar plot demonstrating the distribution of organoids across archetypes. **H)** UMAP from 3M in which color indicates the abundance of each cell type. Each dot represents an individual organoid. Blue indicates few cells of that type are found in that organoid and green indicates high counts for that cell type. RPC_OV: retinal progenitor cell/optic vesicle, RPE: retinal pigmented epithelium, OS: optic stalk, Neuron_NR: non-retinal neuron, RP: roof plate. **I)** UMAP from 2C of the individual clusters used for analyses modeling the variance across treatments and clusters. **J)** UMAP highlighting the clusters with significantly higher variance than expected in None, SAG, All, BMP, CHIR, SU5402, and SU5402:CHIR. **K)** Box plots with clusters ordered according to increasing CV test stat. A single CV test stat is calculated for each treatment, and the boxplots summarize the CV test stat values across treatments for each cluster. Box plots are colored by the cell type assignment as in Figure 2E. RPC_OV: retinal progenitor cell/optic vesicle, RPE: retinal pigmented epithelium, OS: optic stalk, RP: roof plate, FP: floor plate.

—----------

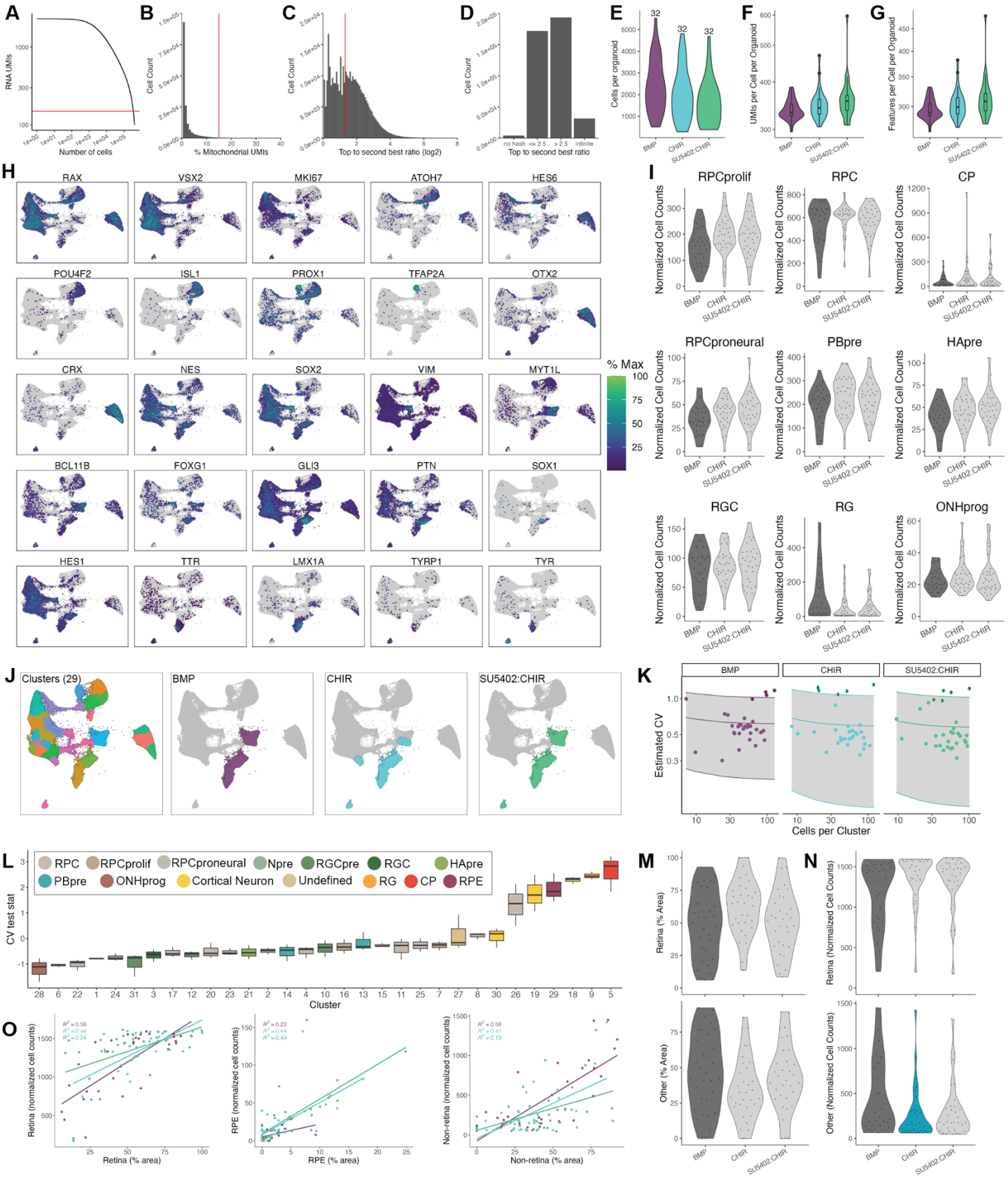
A
RNA UMIs
Number of cells
B
Cell Count
% Mitochondrial UMIs
C
Cell Count
Top to second best ratio (log2)
D
Cell Count
no hash
<= 2.5
> 2.5
infinite
Top to second best ratio
E
Cells per organoid
32
32
32
BMP
CHIR
SU5402:CHIR
F
UMIs per Cell per Organoid
G
Features per Cell per Organoid
H
RAX
VSX2
MKI67
ATOH7
HES6
POU4F2
ISL1
PROX1
TFAP2A
OTX2
CRX
NES
SOX2
VIM
MYT1L
BCL11B
FOXG1
GLI3
PTN
SOX1
HES1
TTR
LMX1A
TYRP1
TYR
% Max
100
75
50
25
I
RPCprolif
RPC
CP
RPCproneural
PBpre
HApre
RGC
RG
ONHprog
Normalized Cell Counts
BMP
CHIR
SU5402:CHIR
J
Clusters (29)
BMP
CHIR
SU5402:CHIR
K
BMP
CHIR
SU5402:CHIR
Estimated CV
Cells per Cluster
L
RPC
RPCprolif
RPCproneural
Npre
RGCpre
RGC
HApre
PBpre
ONHprog
Cortical Neuron
Undefined
RG
CP
RPE
CV test stat
Cluster
28 6 22 1 24 31 3 17 12 20 23 21 2 14 4 10 16 13 15 11 25 7 27 8 30 26 19 29 18 9 5
M
Retina (% Area)
Other (% Area)
N
Retina (Normalized Cell Counts)
Other (Normalized Cell Counts)
O
Retina (normalized cell counts)
Retina (% area)
RPE (normalized cell counts)
RPE (% area)
Non-retina (normalized cell counts)
Non-retina (% area)

Figure S4. Quality control of the D63 organoid datasets, related to Figure 4. A) A knee plot of the number of UMIs per cell compared to the number of cells recovered. The red line (150 UMIs) indicates the value denoting whether a barcode combination should be considered a cell. **B)** A histogram of the number of cells per % mitochondrial UMIs. All cells with > 15% were discarded. **C)** A histogram of the number of cells recovered at each Top to Second Best Ratio was then generated. The red line (2.5) denotes the Top to Second Best Ratio required for a cell to be assigned a confident hash call. **D)** A bar plot of the number of cells with Top to Second Best Ratios matching given criteria. In the event only a single hash barcode is detected, the ratio is infinite. **E)** Violin plot of the number of cells recovered for each organoid across treatments. **F)** Violin plot of the number of UMIs recovered from each cell per D63 organoid per treatment. **G)** Violin plot of the number of features recovered from each cell per D63 organoid per treatment. **H)** Expression plots of the genes used to define cell types in Figure 5A. **I)** Violin plots of size-factor normalized cell counts for D63 organoids. The dark gray indicates the treatment that was used for fold-change calculations in 5B, and light gray indicates no significant change in cell type abundance. **J)** A beta-binomial distribution was used to determine the dispersions across treatments for each of the 29 clusters used to define cell types. The mean and CV calculated from the beta-binomial distribution, were then used to model the relationship between the number of cells per cluster and the CV using a gamma distribution. Left: UMAP with the cells colored by the 29 clusters used to define cell types. Right: UMAPs in which the clusters highlighted are more variable across treatments than expected by chance. Cells are colored by treatment. **K)** Displayed are the modeled relationships between mean cell count and CV per cluster colored by treatment. **L)** Boxplots with clusters ordered according to increasing CV test stat. A single CV test stat is calculated for each treatment, and the boxplots summarize the CV test stat values across treatments. RPC: retinal progenitor cell, RPCprolif: proliferating RPC, RPCproneural: proneural RPC, Npre: retinal neural precursor, RGC: retinal ganglion cell, RGCpre: RGC precursor, HApre: horizontal/amacrine precursor, PBpre: photoreceptor/bipolar precursor, ONHprog: optic nerve head progenitor, RG: radial glia, CP: choroid plexus, RPE: retinal pigmented epithelium. **M)** Violin plots of % Area measurements for Retina and Non-retinal (Other) cell types as calculated from bright phase microscopy images of D62 organoids. Plots are colored as in S6H. **N)** Violin plots of size-factor normalized Retina and Non-retinal (Other) cell counts for D63 organoids using broad cell types. Plots are colored as in S6H with teal indicating a significantly decreased cell type abundance. **O)** Scatter plots showing the correlation between the sci-Plex cell counts and % Area for each individual D63 organoid across treatments. R^2 values are in the top right corner colored by treatment.

—----------

Table S1. Cost benefit analysis between sci-Plex and 10x*, related to Figure 1.

Experiment	Total cells	sci-Plex cost per cell	10x cost per cell	sci-Plex cost per sample prep	10x cost per sample prep
10x match	16,914 (10x) 12,867 (sci)	$0.14	$0.35**	$608	$2000*
D28	203,511	$0.04	$0.30***	$23	$196***
D63	194,335	$0.11	$0.0625***	$76	$232***

* This analysis does not take into account the sequencing cost. However, sci usually results in fewer UMIs which can make it difficult for some gene expression analyses, but it does make it easier to sequence for a lower cost.

**This was the actual cost for the experiment as performed. Each age was loaded onto its own lane with a desired recovery of 7000 cells per well.

***This estimate assumes multiplexing of 16 samples per lane using the CellPlex kit. A desired recovery of 500 cells per sample (8000 cells per lane) was assumed for the D28 experiment and 2000 cells per sample for the D28 experiment (32,000 cells per lane). These values are based off of the median number of cells recovered per organoid from the sci-Plex experiments.

Table S2. Cell type marker genes, related to Figures 1-4.

A list of the genes used to assign cell types for all sci-Plex experiments

Cell Type	Expt	Enriched Markers								
RPC	10x_sci comp	VSX2	RAX							
Proliferating RPC	10x_sci comp	VSX2	RAX	MKI67	TOP2A					
MG	10x_sci comp	RLBP1								
PAX2high RLBP1low	10x_sci comp	PAX2	RLBP1							
Lens	10x_sci comp	PROX1	CRYBB1							
Astrocyte	10x_sci comp	PAX2	GFAP							
Forebrain	10x_sci comp	SOX1	FOXG1							
Neuron nonretinal	10x_sci comp	ELAVL4	DLX6	MYT1L						
Roof plate	10x_sci comp	GDF7	LMX1A							
Npre	10x_sci comp	HES6	ATOH7							
RGCpre	10x_sci	ATOH7	POU4F2							

	comp									
RGC	10x_sci comp	POU4F2	ISL1							
HApre	10x_sci comp	PRDM13	TFAP2A							
Amacrine	10x_sci comp	TFAP2A								
Horizontal	10x_sci comp	PROX1	TFAP2A	ONECUT1						
PBpre	10x_sci comp	HES6	OTX2	CRX						
Cone RG	10x_sci comp	ARR3	CRX	OTX2						
Cone Blue	10x_sci comp	OPN1SW	CRX	OTX2						
Rod	10x_sci comp	NRL	CRX	OTX2						
Unknown	10x_sci comp	PIK3CG	PP1R27	GDF15	KBTBD12	INPP5D	OTX2			
OFF Bipolar	10x_sci comp	VSX1	GRIK1	OTX2						
ON Bipolar	10x_sci comp	VSX2	ISL1	PROX1	GRM6	OTX2				
RPC/OV	D28 All cells	RAX	VSX2	HES1						
OS	D28 All cells	VAX1	PAX2	SOX1						
Telencephalon	D28 All cells	SOX1	FOXG1	NKX2-1						
Diencephalon	D28 All cells	SOX1	FOXD1	NKX2-2						
Hindbrain	D28 All cells	HOXC4	HOXD3	HOXB6						
FP	D28 All cells	FOXA2	SHH							
RP	D28 All cells	GDF7	TTR	LMX1A						
Neuron nonretinal	D28 All cells	ELAVL4	MYT1L	EOMES	FOXG1					
Retina	D28 All cells	RORB	ATOH7	ONECUT2	HES6	RAX				
Cornea	D28 All cells	DCN	LUM							
Lens	D28 All cells	PROX1	CRYBB1							
RPE	D28 All cells	TYRP1	TYR	TRPM1	OTX2					
RPC/OV	D28 Retina	RAX	VSX2	HES1						
Npre	D28 Retina	HES6	ATOH7							
RGCpre	D28 Retina	ATOH7	POU4F2	ISL1						
HApre	D28 Retina	TFAP2A	PRDM13							
PBpre	D28 Retina	OTX2	CRX							

RPC	D63	RAX	VSX2	RORB						
RPCprolif	D63	RAX	VSX2	MKI67	TOP2A	RORB				
RPCproneural	D63	MKI67	TOP2A	ATOH7	HES6	RORB	ONECUT1			
Npre	D63	ATOH7	HES6	RORB	ONECUT1					
RGCpre	D63	ATHO7	POU4F2	RORB	ONECUT1					
RGC	D63	POU4F2	ISL1	RORB	ONECUT1					
HApre	D63	PROX1	TFAP2A	PRDM13	RORB	ONECUT1				
PBpre	D63	OTX2	CRX	ONECUT1	RORB					
ONHprog	D63	NES	SOX2	VIM	SOX1	RAX	VSX2	MKI67	TOP2A	RORB
Transition	D63	N/A								
Cortical Neuron	D63	MYT1L	BCL11B							
Radial Glia	D63	GLI3	FOXG1	SOX1	PTN	SOX2	HES1	PPRX1	OTX1	
Choroid Plexus	D63	TTR	LMX1A	WNT2B	WNT3A	OTX2				
RPE	D63	TYRP1	TYR	OTX2	MITF					